



**DEVELOPMENT AND CHARACTERIZATION OF
A PLASMA-NEEDLE
FOR BIOMEDICAL APPLICATIONS**

Diploma thesis

by

Matthias Bäcker

August 2007

First examiner : Prof. Dr. Mattea Müller – Veggian

Second examiner: Prof. Dr. Michael J. Schöning

Supervisors : Prof. Vincenzo Palmieri, Dott. Niccolò Patron

**The experimental work of this thesis was executed at the
superconductivity laboratory at the Legnaro National Laboratories,
Istituto Nazionale di Fisica Nucleare.**

Table of contents

1 Einleitung.....	5
1.1 Introduction.....	6

PART I

2 Literature review	9
2.1 Biomedical applications of plasmas	9
2.2 Surface modification.....	12
2.3 Carbon film deposition	13
2.3.1 Carbon layers for biomedical purposes.....	13
3 Plasma fundamentals.....	18
3.1 Plasma.....	18
3.1.1 Collision processes in plasmas.....	20
3.1.2 Common regimes for driving a plasma	22
3.1.2.1 Microwave regime.....	23
3.1.2.2 Radio-frequency (RF) regime.....	25

PART II

4 Experimental procedures and tools.....	29
4.1 Experimental setup	29
4.1.1 Estimation of the cyclohexane content.....	33
4.2 Plasma diagnostics.....	34
4.2.1 Voltage and current measurements	34
4.2.1.1 Probe calibration.....	37
4.2.2 Langmuir probes	38
4.2.3 Optical emission spectroscopy	40
4.3 Surface modification experiments	40
4.3.1 Contact angle measurements.....	40
4.3.2 Enzyme-linked immunosorbent assays (ELISA)	42
4.4 Carbon film deposition	43
4.4.1 Profilometry	43
4.4.2 Fourier transform infrared spectroscopy (FTIR).....	44
5 Results and discussion	50
5.1 Characterization of the plasma-needle.....	50
5.1.1 Electrical measurements.....	50
5.1.1.1 Breakdown voltage and U-I characteristic	50
5.1.1.2 Determination of the resistive power dissipation	51
5.1.1.3 Error analysis.....	53
5.1.2 Temperature measurements.....	54
5.1.2.1 Pure helium plasma	55
5.1.2.2 Helium – cyclohexane mixture plasma	56
5.1.3 Optical emission spectroscopy	57

PART III

5.2 Plasma-needle applications.....	61
5.2.1 Surface modification	61
5.2.1.1 Contact angle measurements of various substrates after helium plasma treatment.....	61
5.2.1.2 ELISA results	64
5.2.2 Carbon film deposition.....	66
5.2.2.1 Profiles and deposition rates.....	66
5.2.2.2 FTIR	69
6 Conclusions.....	72
6.1 Zusammenfassung	74
Acknowledgement	76
Bibliography	77
List of tables	81
List of figures	82

Meiner Familie

1 Einleitung

Plasmen finden aufgrund ihrer speziellen Eigenschaft zunehmend Verwendung in der biomedizinischen Technik. Anwendungsmöglichkeiten erstrecken sich über Oberflächenmodifikation von Implantaten und Instrumenten durch Plasmaaktivierung oder gezielte Schichtabscheidung von diamantähnlichen und biokompatiblen Strukturen zu gänzlich neuen Anwendungsmöglichkeiten im Bereich der Interaktion mit biologischem Gewebe und einem Plasma selbst.

Plasmen bei Atmosphärendruck haben gegenüber Niederdruckplasmen den entscheidenden Vorteil, dass sie ohne kostenintensive Vakuumtechnik erzeugt werden können. Die physikalischen Eigenschaften ändern sich allerdings signifikant mit zunehmendem Druck, weswegen das Interesse an sogenannte Mikroplasmen in den vergangenen Jahren stark gestiegen ist. Diese können stabil bei Atmosphärendruck ohne Bildung von Lichtbögen betrieben werden, sind allerdings in ihrer Größe beschränkt. Lichtbögen können Temperaturen von einigen tausend Grad erreichen und sind deshalb unerwünscht. Das Zusammenschalten von vielen Mikroplasmen zu Plasmenarrays kann gegebenenfalls die begrenzte Wirksamkeit einer einzelnen Plasma-Nadel kompensieren. Die niedrige Hintergrundgastemperatur bei vergleichsweise hoher Elektronendichte solcher Plasma-Nadeln eröffnet ein breitgefächertes Anwendungsspektrum.

Ziel dieser Arbeit war die Entwicklung eines Atmosphärenplasmas, um dessen mannigfaltigen Anwendungsmöglichkeiten mit Schwerpunkt auf biomedizinischen Anwendungen zu untersuchen. Aufbauend auf bereits entwickelte Mikroplasmen und Vorversuchen wird eine Plasma-Nadel entwickelt, die anschließend anhand erster Experimenten charakterisiert und deren Anwendungsmöglichkeiten auf den Gebieten der Schichtabscheidung und Oberflächenmodifikation veranschaulicht worden sind. Weiterführende Versuche zur Interaktion zwischen Plasmen und biologischem Gewebe/Zellen offerieren zukünftigen Forschungsbedarf.

Zunächst wird ein Überblick über den Stand der Technik und Forschung im Bereich der Mikroplasmen vermittelt und Anwendungsmöglichkeiten im Bereich der biomedizinischen Technik erläutert. Die daran anschließenden Kapitel beschreiben die Grundlagen der Plasmaphysik sowie den Aufbau und das Funktionsprinzip der Plasma-Nadel. Des Weiteren werden die unterschiedlichen zur Anwendungen kommenden Diagnosemethoden dargestellt. Die Präsentation und Interpretation der erzielten Messergebnisse sind Gegenstand des fünften Kapitels.

1.1 Introduction

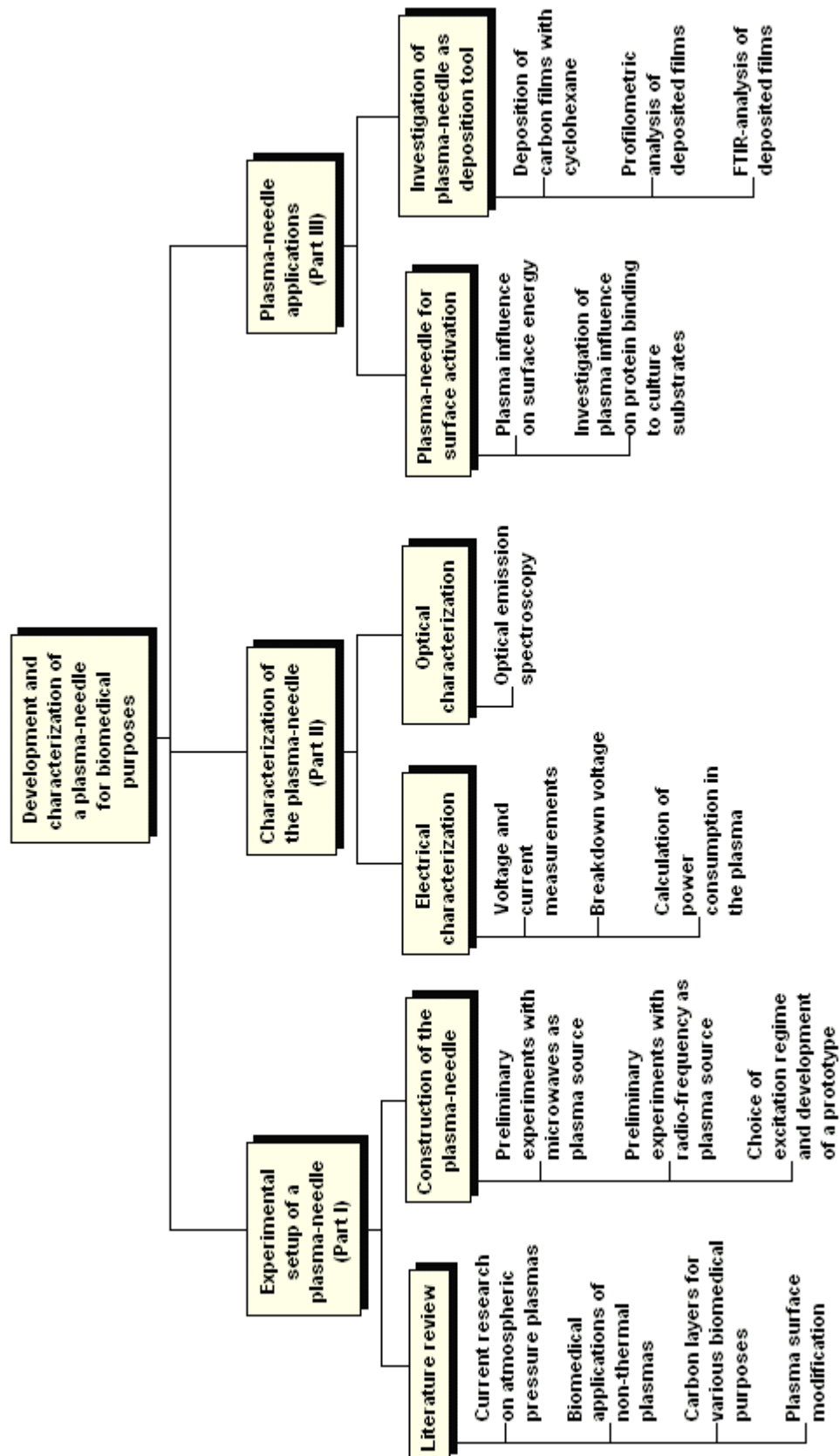
Due to their unique properties, plasmas have found a broad range of applications in biotechnology and biomedicine, including surface modification of implants and instruments by plasma activation or the deposition of specific diamond-like- and biocompatible structures. A completely new field is the investigation of plasma interaction with biological tissues and the exploration of potential applications.

In contrast to low pressure plasmas, atmospheric pressure plasmas can be operated more conveniently at ambient air and do not require costly vacuum systems. However, the physical properties of a plasma alter significantly with increasing pressure. Therefore, there is a steadily increasing interest in plasma-needles in recent years. These plasma-needles operate stably at atmospheric pressure without producing (filamentary) arcs, but are restricted to their size. Arcs can develop temperatures of several thousand degrees Kelvin and are therefore undesired. The construction of plasma-needle arrays can compensate the reduced effectiveness of a single plasma-needle. The low temperature of the background gas and comparable high electron density of such plasma-needles offer manifold applications.

The objective of this work is the setup of a new atmospheric plasma device for the exploration of its diverse applications with focus on biomedical applications. With the help of comparable work and on the basis of preliminary experiments, a new plasma-needle has been fabricated. Subsequent, that plasma-needle was initially characterized and experimentally tested for thin film deposition and surface modification and is ready for tests on bacteria inactivation.

At first, a review of the state-of-the-art and current research on plasma-needles and their biomedical applications is given. The following two chapters deal with the basics of plasma physics, the experimental setup and the diagnostic tools as well as the principle of the plasma-needle. The results of the different measurements are presented and discussed in chapter five.

The following diagram is intended to help understanding the different steps of the work progress. After an introductory literature review, preliminary experiments with different plasma sources were executed. Thereupon, a prototype was constructed, which then was characterized and tested on two different possible applications, surface activation and carbon film deposition.



PART I

2 Literature review

2.1 Biomedical applications of plasmas

In recent years, researchers and plasma physicists turned from plasma applications, like surface modifications and thin film deposition for biomedical applications towards leveraging the unique properties of the plasma *itself*. Years of research in plasma physics led to a considerable expertise in plasma-material processing. The next logical step is utilizing and expanding this existing knowledge in a new area of research, the biomedical research. Non-thermal plasmas are unique objects that combine high reactivity with non-destructive characteristics. One important feature is that plasmas act specifically on the surface, with a minimal penetration depth, and provide active species (radicals, ions, UV-photons) for specific modification. This properties offer the application of non-thermal plasmas for non-contact medical treatment. This treatment is local, fast, does not require toxic substances, does not cause heating damage or produces debris. Plasma-based tools cannot perform bulk surgery, but they may be extremely useful in therapies, which require refined action on the outer layers of the tissue. Plasma treatment is fundamentally different from currently used laser surgery, because laser radiation penetrates the tissue and causes heating and cell destruction. Due to the flexibility of plasmas, which can be easily confined within catheters, minimum-invasive treatment of difficult to access places, like blood vessels, dental cavities and intestines can be performed. One can think of numerous processes, like removal, (de)activation, and changing the functionality of cells or tissues. This may find application in the treatment of various skin ailments, hair growth restoration by activation of hair bulbs, etc. Plasma technology also promises a breakthrough in dentistry, as a novel method of cleaning dental cavities. Unlike the traditional mechanical cleaning using a drill, plasma treatment is expected to be painless and far less destructive, since no heating and vibrations, which irritate the nerve, occur. Plasmas can easily penetrate cavities and act strictly on the surface, so that high-precision cleaning can be performed without excessive removal of healthy pulp. Apart from plasma applications in external skin- and tooth-healing, numerous plasma techniques can be introduced in internal medicine, e.g. to induce cell death in cancer cells.

However, the impact of non-thermal plasmas on organic materials is an entirely new area of research which is barely explored yet. Fundamentally, challenging problems are related to the interaction of plasmas with living tissues. Since plasma is essentially a gaseous medium, while tissues contain aqueous solutions, the contact between these ob-

jects must be investigated. Much research effort has been devoted to plasma-solid surface interactions. However, data on the plasma-liquid interface are rare. The behavior of the plasma in the vicinity of liquids, the penetration of active plasmas species into organic matter and the response of the tissues on the cellular level belong to the most intriguing questions. In plasma processing of *solid-state* material the action of a plasma is versatile. Dependent on the chosen plasma type and conditions, many different results, like selective cleaning/etching, surface activation and deposition of thin layers can be achieved. In processing of *organic* matter and tissue, the additional complexity is introduced because of the yet unknown biochemical response of the treated object. Efficiency and selectivity with respect to various kinds of material, i.e. tissues have to be investigated. Furthermore, it is important to understand the role of various active plasma species. Radicals, ions and (UV-) photons will have different impacts on organic molecules. Although not all plasma-induced effects are easy to predict, several types of cell modification can possibly be achieved. The simplest and most drastic one is the cell destruction, which has already been demonstrated in plasma-assisted coagulation and sterilization techniques. This action can be compared with non-selective etching in solid-state processing, and this also constituted the first level of plasma usage in the history of material science. If the analogy between inorganic and organic material processing retains, one can expect much more sophisticated plasma-tissue interactions than the mere cell destruction. Thus, it has to be studied whether the cell interior can be modified selectively without affecting the cell membrane, whether the membrane can be locally removed or modified in order to, for example, alter its permeability for a given kind of pharmaceutical, and if plasma treatment can be restricted to one cell layer without affecting the rest of the (healthy) tissue.

Investigating and answering these questions demands the joint expertise of plasma physicists, cell biologists, cell biophysicists, and medical researchers. Further specialised expertise is required as soon as it comes to customization of plasmas for special applications, for example expertise on cardiovascular biology in case of artery treatment.

Concluding, biomedical plasma technology is an unexplored area with a great potential in medical sciences. Due to their unique physical nature, plasmas have the potential to become a novel medical technique: they will act on the tissue surface with high precision and minimum penetration whilst providing active species for refined cell modification. However, plasmas must satisfy strict requirements in order to be applied on biomedical purposes. They have to be operated at atmospheric pressure and should not cause any damage to biological tissue due to an electric shock, thermal damage, or any other yet un-

known effect. The state-of-the-art on plasma sources and plasma generation technology offers different methods of excitation ((pulsed) DC-, radio-frequency, or microwave-excitation) and geometric designs (coaxial electrode configuration, a virtual counter-electrode configuration with the surrounding acting as ground, dielectric barrier discharge) yielding plasmas with different properties. Each of those approaches has its advantages and drawbacks. However, in the end, the plasma's prospective applications require low dimensions, stable plasma generation, sufficient active plasma species production, and the satisfaction of the safety requirements mentioned above. More and more research groups have started developing plasma devices and are experimenting on their applications. Examples of already available plasmas and current research on their medical applications are given below¹:

STOFFELS ET AL. [1] have developed a plasma-needle operating at atmospheric pressure that offers a broad range of biomedical applications. Due to the small size of the discharge (approx. 1 mm in diameter) and the comparable low power consumption, the plasma-needle operates near room temperature causing no thermal damage to biological tissue. This plasma-needle has already been successfully tested on killing of *Escherichia coli* bacteria during in-vitro studies [2]. Samples that were exposed to the plasma showed a characteristic circular- and sharp-edged void in the bacteria lawn after within less than one minute. It is assumed that the short-living reactive species (O , OH^- , HO_2^-) created by the plasma are responsible for the bacteria deactivation, although the mechanism is not completely understood, yet. Further studies on Chinese hamster ovarian cells (CHO-K1) and human cells of lung carcinoma (MR65) have revealed another effect of a plasma-needle on cell cultures: cell detachment [3]. A plasma-induced destruction of cell adhesion molecules was made responsible for the temporary loss of the inter-cell-contact and detachment from the substrate while the cells remained alive. It is believed that this effect could be leveraged for future applications in microsurgery and accelerated wound healing. Since the cell membranes remained undamaged and the detached cells were not necrotic, inflammation² is prevented. Furthermore, it is proposed that this effect could be used as a complementary treatment to percutaneous coronary intervention [4].³ At present, the most promising application of the plasma-needle is the deactivation of dental bacteria. A study on the effects of plasma on the most significant cariogenic micro organism, *Streptococcus*

¹ The description of this application was written on the basis of E. Stoffels research outline and on the basis of her talk at the LNL on June 29th, 2007.

² The release of cytoplasm into the interstitium due a damage of the cell membrane would induce an inflammatory reaction in the tissue.

³ Percutaneous coronary intervention is an invasive cardiologic therapeutic procedure to treat the stenotic coronary arteries.

plasma on the most significant cariogenic micro organism, *Streptococcus mutans*, produced promising results [5]. In contrast to drilling or using chemotherapeutic agents, plasma treatment offers certain advantages: it can kill the *Streptococcus mutans* bacterium, it is a painless procedure, the treatment is site-specific, and no excess radicals remain.

Other groups used atmospheric pressure plasmas in a closed chamber for successful deactivation or killing of further bacteria and additionally fungi, viruses, and endospores [6].

FRIDMAN ET AL. [7] reported the successful killing of Melanoma skin cancer cells by means of a dielectric barrier discharge operating at ambient air. Depending on the treatment dose, cells were killed by necrosis⁴ or apoptotic⁵ behaviour that was initiated by the plasma treatment leading to cell death after 12 to 24 hours. This initiation of apoptosis is of high value for cancer treatment, since “*cancer cells frequently have acquired the ability to block apoptosis and thus are more resistant to chemotherapeutic drugs*” [7].

2.2 Surface modification

The presence active species (ions, electrons, radicals, and metastables) in a plasma and the emission of UV-light allows surface modification. The energetic species in a plasma bombard a surface that is in contact with the plasma. Their energy is transferred to and dissipated within the substrate by a variety of chemical and physical processes. Surface functionalization, adhesion promotion, molecular immobilization, enhanced surface wettability, and improved biocompatibility are some of the possible and desired results of those processes. The great advantage of plasma surface modification is that plasma treatment only modifies the nearby substrate and does not change the bulk material. Furthermore, almost every substrate geometry can be treated. Plasmas operating near room temperature do not damage the biomaterials, which are in most cases heat-sensitive. The broad range of possible plasma processes varying in treatment power and treatment time, gas type, and pressure allows customized application in biomedicine. Hydrophilic and hydrophobic surfaces can be created on polymers through interaction with plasma. Hydrophilicity refers to the physical property of a molecule or surface that can bond with water or other polar solvents through hydrogen bonding. Hydrophobic molecules or surfaces tend

⁴ Necrosis is the death of cells in an organ or tissue, caused by disease, physical or chemical injury, infection, or inflammation.

⁵ Apoptosis is a type of cell death in which the cell uses specialized cellular machinery to kill itself.

to be non-polar and thus prefer other neutral molecules and non-polar solvents. Hydrophobic molecules often cluster together in water, e.g. a drop of grease. Using oxygen to create hydrophilic functionality increases the wettability of a surface. Furthermore, the active oxygen species combined with UV-energy create a chemical reaction with the surface contaminants, resulting in their volatilization and removal from the surface.

BRINEN ET. AL [8] reported that contact lenses and intraocular lenses have been successfully modified by plasma treatment to decrease bacterial adhesion and improve wettability while enhancing patient comfort.

Improving adhesion between two surfaces is another common application. Good adhesion requires strong interfacial forces. Plasma treatment has been employed to modify the surface of metal implants for adhesion promotion to bone cements or to enhance cell attachment and growth [9].

The surfaces of culture substrates, for example petri dishes, micro-carriers and membranes can be modified by plasma treatment to improve cell growth, protein binding or non-binding, improve hemocompatibility and cell-specific attachment by controlling the chemical structures of the surfaces. Adding amine functional groups to a biomaterial which encounters blood can improve hemocompatibility. The amine groups are attached by ammonia plasma treatment. They act as hooks for anticoagulants, such as heparin, and thereby decrease the thrombogenicity [10].

2.3 Carbon film deposition

Another potential application for plasma-needles is the deposition of thin films. With emphasis on material coatings for biomedical applications, diamond-like carbon coatings have drawn a lot of attention in recent years [11]. The term diamond-like carbon (DLC) is often misused. It is an umbrella term referring to different forms of amorphous carbon materials that display some of the properties of natural diamond.

2.3.1 Carbon layers for biomedical purposes

Carbon is the first element of the fourth group in the periodic table. It exhibits four valence electrons and is the smallest atom of the fourth group. The four valence electrons of the carbon atom can contribute to forming a crystal lattice in different ways. Depending on whether all four, three, or just two electrons are hybridized, different lattice characteris-

tics are obtained. sp^3 -hybridization (as in diamond) consists of four strong covalent σ -bonds in a tetragonal arrangement. The atoms arrange in a spatial lattice as shown in figure 1, giving diamond its high hardness. A sp^2 -hybridized carbon atom (as in graphite) has three trigonal arranged σ -bonds and one π -bond, which is based on van-der-Waals forces and therefore significantly weaker. The atom network appears as a plane structure as seen in figure 1. Although the bonds within a graphite *layer* are stronger than in diamond, the forces between two graphite layers are comparably weak (π -bonds). Therefore, graphite layers can slip over each other, making them smooth. Due to their electrical conductivity, graphite layers are used in the electrical industry and for the sample preparation of scanning electron microscopy. sp^1 -Hybridization (as for example in polyethylene) means bonding with two σ -bonds and two π -bonds, forming a linear chain.

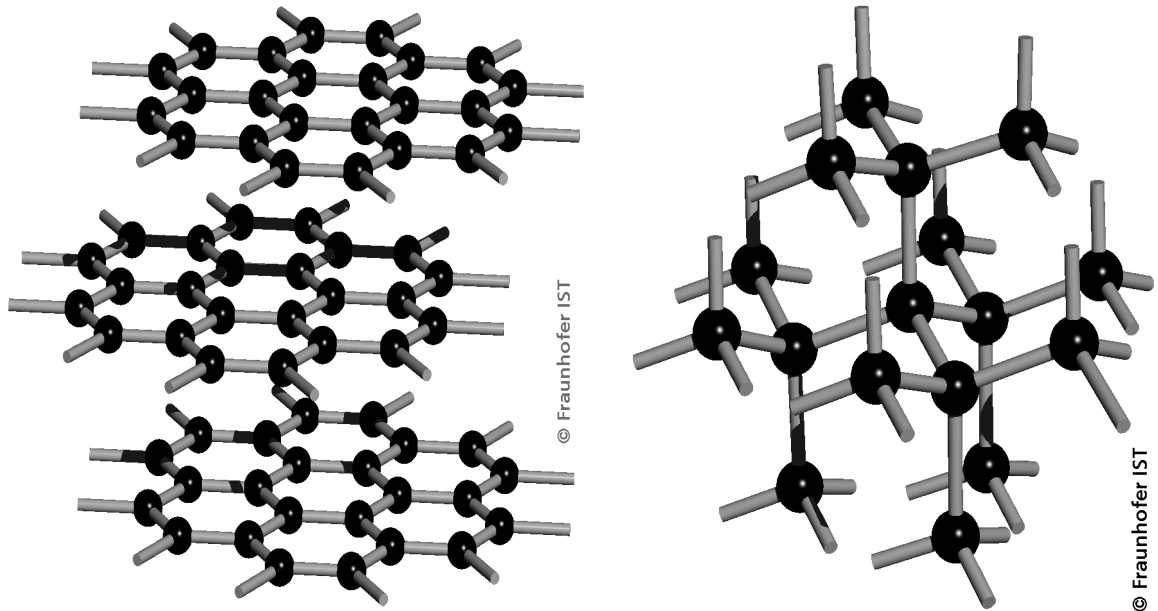


Fig. 1: Crystal lattice of diamond (left) and crystal lattice of graphite (right)⁶

However, it is rather difficult and expensive to create pure diamond layers artificially and in many cases not necessary. Adding of hydrogen or metals reduces production expenses but also alters the properties of the layer. Depending on its sp^3 , sp^2 , and hydrogen content, coatings have a wide range of properties. In general, one can say that if the sp^2 -type is predominant the film will be softer, if the sp^3 -type is predominant, then the film will be harder. Figure 2 shows the ternary phase diagram of amorphous carbon.

⁶ By courtesy of Fraunhofer-IST, see appendix.

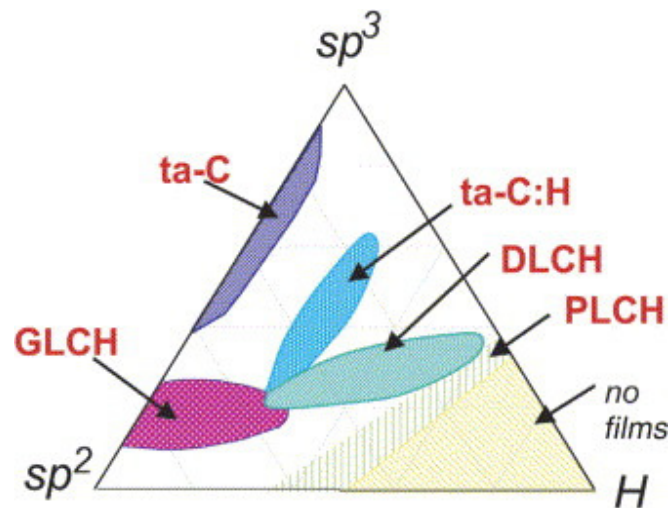


Fig. 2: Ternary phase diagram of amorphous carbon⁷

The three corners correspond to diamond, graphite, and hydrocarbons, respectively. Depending on the sp^3 -content and H-content, DLC can be classified as summarized in table 1.

Tab. 1: Classification of different diamond-like carbon films

Abbr.	Name	sp^3 - content	Hydrogen-content
ta-C	Tetrahedral amorphous carbon	>60%	0%
PLCH	Polymer-like hydrogenous amorphous carbon film	>40%	Up to 70%
DLCH	Diamond-like hydrogenous amorphous carbon film	<70%	20-40%
GLCH	Graphite-like hydrogenous amorphous carbon film	<20%	<20%
ta-C:H	Tetrahedral amorphous carbon with hydrogen	Up to 70%	25-35%

Bioimplants require a lot of special material properties: they should not cause infections or inflammations, prevent uncontrolled cell growth, maintain integrity inside the body, avoid formation of debris, and be non-toxic and non-carcinogenic. Some applications also require hardness, wear resistance, and a low friction coefficient. These require-

⁷ Graph and its description taken from Cinzia Casiraghi, John Robertson, and Andre C. Ferrari. Diamond-like carbon for data and beer storage. In: *Materials Today Jan-Feb 2007 / Vol. 10 / Number 1-2*.

ments can be conformed with special surface properties, since ultimately it is the implant's surface interacting with the surrounding cells and body fluids. Common materials that are used for biomedical applications are titanium, 316 stainless steel, titanium nitride, cobalt-chromium alloys, and nitinol alloys. However, there are some drawbacks that these materials suffer from, for example, release of metal ions, corrosion, cytotoxicity, and wear. Since the metal ions and other particles released from implants are suspected to trigger allergic reactions, there is growing interest in less corrosive and inert biomaterials. Owing to its tribological and mechanical properties, its high wear- and corrosion resistance, biocompatibility, and hemocompatibility⁸, DLC has emerged as a promising material for orthopaedic, cardiovascular, dental, ophthalmological, and urological applications.

LAUBE ET AL. [12] reported that covering of urological indwelling catheters with an amorphous hydrogenous carbon (a-C:H) film reduced urinary tract infections significantly, improved the handling, and caused less pain during replacement. Furthermore, in contrast to uncoated stents, no encrustations of crystalline bacterial biofilms⁹ were observed.

There are publications discussing the impact of different DLC-coatings on contact lenses [13, 14]. Depending on the kind of DLC-coating results comprise enhanced stability, minimized UV-transmission, elongated lifetime, reduced antibacterial activity and inflammatory processes, and a higher refractive index, which enables the reduction of the lenses' thickness.

Besides coating of artificial heart valves and pacemakers, which require hemocompatible, and in case of pacemakers also conductive surfaces for the leads, the main cardiovascular application is the modification of (coronary) stents. A stent denotes a metal tube permanently inserted into an artery. It is used to reopen an artery suffering from atherosclerosis and sustain sufficient blood flow. The main side effect of a stent-implantation lies in its release of metal ions and its thrombogenicity. Both effects can be diminished with a DLC-coating. It should be noted that the DLC-coating has to maintain its integrity during expansion of the stent [15].

Orthopaedic applications include coating of the articular surface of prosthetic joints. These surfaces must bear comparable high loads giving rise to wear and corrosion due to exposure to synovial fluid. The debris formation as a consequence of the wear can cause inflammation and finally lead to loosening of the implant. DLC with its high hard-

⁸ Hemocompatibility refers to the compatibility of non-physiological surfaces in contact with blood.

⁹ These biofilms can cause severe complications and microbial infections.

ness, corrosion resistance, low frictional coefficient and biocompatibility offers a possible solution for improving the present situation [16].

Current research focuses on the effects of incorporation of various elements to DLC-coatings in order to obtain further improvements of the film's properties. For example, the incorporation of fluorine in a-C:H films that significantly reduced the thrombogenicity. Furthermore, the addition of silicon increased the substrate adhesion and reduced the film cracking [11].

3 Plasma fundamentals

3.1 Plasma

Plasma is an electrically conductive gas containing charged particles. In general, plasmas are generated by supplying energy to a neutral gas giving rise to the formation of charge carriers. Electrons and ions are produced in the gas phase when electrons with sufficient energy collide with neutral atoms and molecules in the carrier gas. This and other collision processes occurring in a glow discharge will be discussed in chapter 3.1.1.

Plasmas can be divided into local thermodynamic (or thermal) equilibrium (LTE) plasmas and non-local thermodynamic equilibrium (non-LTE) plasmas.

The temperatures of electrons, ions, and neutrals are not inevitably equal. If electrons and ions have the same temperature, i.e. they are in thermal equilibrium, the plasma is classified as thermal. The temperatures of the electrons and the heavy particles can reach some thousand degrees Kelvin and high electron densities of 10^{21} - 10^{26} m⁻³ are observed [17]. A typical example for such a LTE-plasma is an atmospheric arc. At lower pressure, the electrons can gain much more energy than the ions and neutrals because of the greater mean free path. Due to the low frequency of elastic collisions between electrons and atoms, the electrons do not have much possibility to convey their energy to the background gas atoms. In contrast to the electrons, which typically have an energy of several electron volts, the temperature of the background gas does not exceed ambient temperature significantly. Hence, these plasmas in non-thermal equilibrium are of specific interest for technological applications. Typical applications for material processing are, for example, etching, cleaning, or coating. With increasing pressure the mean free path decreases, leading to more frequent collisions between electrons and the heavy particles. Therefore, the electrons gain less energy during their acceleration between the collisions but can convey this energy more easily to the heavy particles. Figure 3 [18] illustrates this dependence between electron- and heavy-particle-temperature and pressure.

In order to generate non-thermal plasmas for technological applications the pressure has to be reduced, which is achieved by using comparatively expensive vacuum technology. Since reducing instrument and operating costs is always desirable, another approach to generate non-thermal plasmas at high pressure is to decrease their size. If the discharge volume is kept small, the comparable high surface can conduct the heat more easily to the outside, and the gas heating is limited.

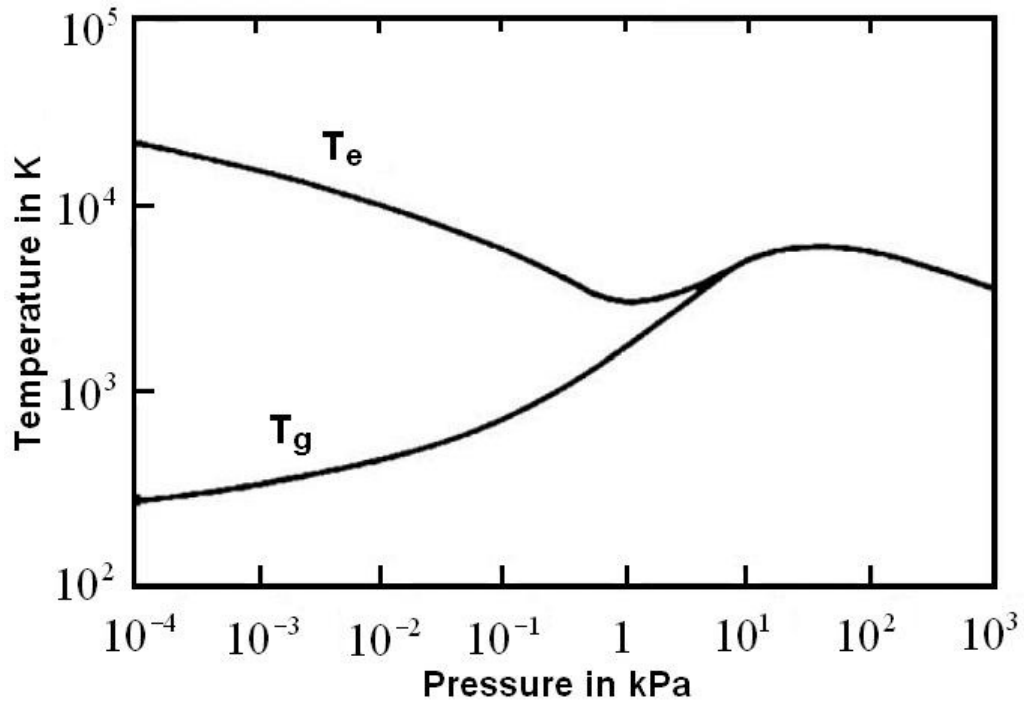


Fig. 3: Dependence between plasma temperature and pressure

Furthermore, the choice of discharge gases influence the thermal properties of the plasma since they differ in their specific heat conductivity. Table 2 lists the heat conductivity of the most common discharge gases.

Tab. 2: Heat conductivity of different gases

Gas	Hydrogen	Helium	Oxygen	Nitrogen	Argon
Heat conductivity[W/(m · K)]	0.18	0.144	0.023	0.02	0.016

In order to ignite the plasma, the gas has to be ionized. When atoms of a gas are excited above a gas-specific energy level, the atoms loose hold of some of their electrons and become ionized. This ionization can be achieved by applying an electric field to the gas. Other options are the supply of thermal energy by use of an exothermic chemical reaction, beams of neutral particles or adiabatic compression until the gas contains enough energy to generate a plasma [18]. Plasma generation by means of an electric field can be divided into direct current (DC) -, pulsed current -, radio-frequency (RF) -, and microwave discharges. In case of an electric discharge, the necessary breakdown voltage is described by Paschen's law:

$$V \approx B \cdot p \cdot d \approx const. \quad (1)$$

With V being the breakdown voltage, p the pressure, d the distance between the electrodes and B a gas-specific parameter, which contains the ionisation energy.

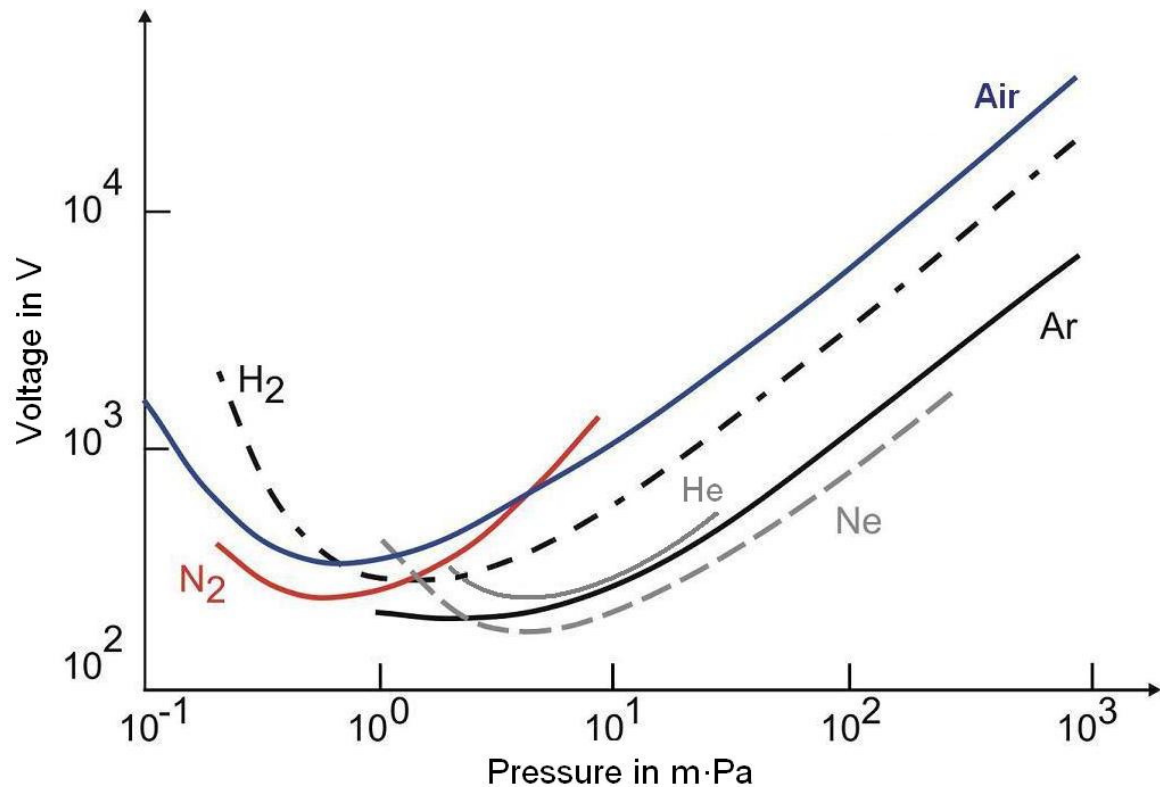


Fig. 4: Paschen's curves for different gases

Figure 4 shows the Paschen graphs for the most commonly used carrier gases helium, nitrogen, argon, neon and hydrogen. The minimum of each Paschen graph is of particular interest, since the breakdown voltage is smallest at this condition. With decreasing pressure or electrode gap the breakdown voltage is increasing rapidly due to the higher mean free path way of the electrons. This diminishes the probability of collision and thus the creation of new charge carriers. With increasing pressure or electrode gap the breakdown voltage is also increasing. But in that case the mean free path way of the electrons is reduced giving rise to much more collisions. However, the electrons are not able to gain enough energy between two collisions that is necessary for further ionization.

3.1.1 Collision processes in plasmas

In principle, collisions between all possible pair permutations are occurring in a discharge, i.e. all particles in a discharge collide with each other, regardless whether both

or only one collision partner are positively or negatively charged or charge-less. Since the collisions involving electrons are dominant in determining the behaviour of the discharge, the discussion is focused on these processes.

Elastic collisions: If an electron is accelerated between two points of potential difference x Volts, then by definition it gains x electron volts or $x eV$ of kinetic energy with e being the electron charge of $1.609 \cdot 10^{-19}$ Coulomb. In case of an elastic collision, the kinetic energy of the colliding particles is conserved. Since the mass of an electron compared to the mass of any atom is some degrees of magnitude smaller the transfer of energy is negligible. Hence, the colliding atom is unaffected and the electron just changes direction without changing its speed significantly. All other types of electron collisions are inelastic.

Ionization: The most important collision process in sustaining the glow discharge is electron impact ionization. The external electric field accelerates a primary electron which then collides with an atom, removing one of its electrons:



Both electrons can then be accelerated repeatedly until they can produce new ionization. In order to remove the most weakly bound electron of a gas atom a minimum energy level is required. This ionization potential differs from gas to gas.

Excitation: If the colliding electron does not have sufficient energy for ionizing the atom, the collision may end up with what is termed excitation. Absorbing just a quantum of energy, an electron is enabled to jump to a higher energy level within the atom. As expected, the threshold for excitation, the excitation potential, is somewhat smaller than for ionization since the electron is not able to completely loose hold of the atom. The excitation potential differs from atom to atom. The excited atom is conventionally represented by an asterisk superscript:



The primary electron loses energy equal to the excitation potential. Some excited atoms have very long lifetimes and are therefore termed metastables excited atoms or just metastables.

The inverse process of excitation is called relaxation. The excited state of an atom is rather unstable. Therefore, the electron configuration soon returns to its initial state by

emission of a photon. The energy difference between the excited and the initial state correlates linearly with the frequency of that emitted photon according to the following equation:

$$E = h \cdot f \quad (4)$$

with E being the energy, h the Planck quantum of $h = 6.626 \cdot 10^{-34} \text{ Js}$ and f the frequency. Since the quantum level of energy is different for each atom, optical emission spectroscopy is very useful for detecting and determining the presence of various atoms in the glow discharge.

The inverse process of ionization is recombination. An electron reunites with a positive ion forming a neutral atom. It is essential for sustaining the glow discharge that the ionization rate is higher than the recombination rate.

Dissociation is the breaking apart of a molecule. A nitrogen-molecule, for example, can be dissociated into two nitrogen atoms. Dissociation can occur by electron impact with energy in excess of the bond strength in the molecule.



The reaction products are generally more reactive than the parent molecule. Thus, dissociation results in an enhancement of chemical activity of the plasma. This mechanism is utilized for the deposition of thin films via plasma-enhanced chemical vapour deposition. The hydrogen and carbon containing precursor gas molecules are dissociated and the new formed species eventually deposit on the substrate forming a thin layer.

In contrast to the noble gases which already have a completely filled outer electron shell, halogens have high electron affinities. Therefore, there is a possibility that an electron colliding with a halogen atom might form a negative ion. This process is termed electron attachment.

3.1.2 Common regimes for driving a plasma

As mentioned in chapter 3.1 there are several methods for the generation of plasmas. However, the most commonly used method is applying an electric field to a neutral gas. The following chapter comprises a further detailed description of two different approaches.

3.1.2.1 Microwave regime

The frequency in the microwave range that has been reserved by the International Telecommunication Union (ITU) is 2.45 GHz with a corresponding wavelength in vacuum of $\lambda = 12.24 \text{ cm}$. In order to minimize distortion of broadcasting signals, specific frequencies have been reserved for scientific, technical, and medical purposes. Other than 2.45 GHz are, for example, 13.56 MHz and its higher harmonics (27.12 MHz, 40.68 MHz, and 54.24 MHz). In contrast to RF, the microwaves are not transmitted by means of a coaxial cable but by (rectangular) waveguides. These allow a higher power transmission. One dimension of the cross-section has to be shorter than the wavelength of the frequency that has to be transmitted. Hence, the electromagnetic waves only match the waveguide when propagating in a zigzag movement directing towards the tube to the load. Due to the quickly changing electric field the amplitude of the electron oscillation is very small. High energy densities are achievable with microwave discharges.

During this work preliminary experiments with microwave-generated plasmas were performed. The figures (5-7) below depict different development stages. The initial device consisted of an approximately 8 cm long stainless steel cylinder with an inner diameter of 10 mm. The cylinder acted both as ground and as shield against the microwaves. The device was driven by a Switching Power Generator SM 445 by Alter Power Systems. A copper antenna with a diameter of 3 mm was inserted and connected to the microwave port. Helium was flooded into the inter-electrode space. To prevent excessive heating the cylinder was water-cooled.

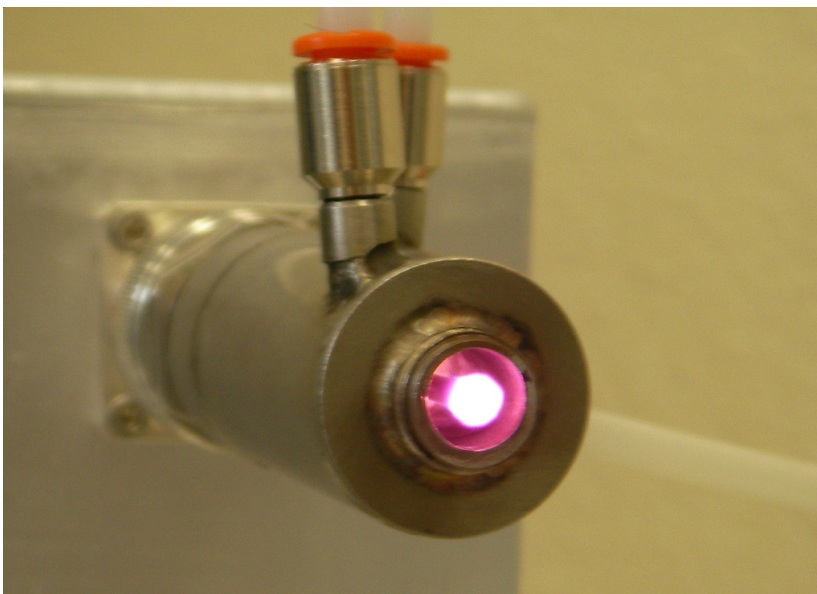


Fig. 5: Preliminary experiments with microwaves

With an additional insulation of the copper electrode arcing was prevented and thereby the device could be operated with more forward power giving rise to the formation of a plasma jet as seen in figure 6.

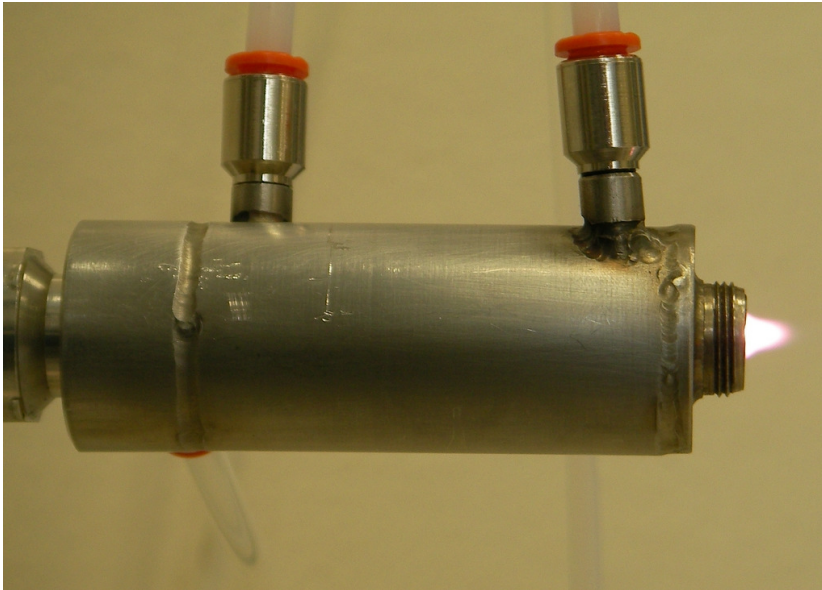


Fig. 6: Microwave driven plasma-jet formation at higher power

A stainless steel rod protruding from the grounded cylinder, which was surrounded by a Plexiglas tube to channel the helium flow, enabled the generation of the plasma outside of the cylinder as presented in figure 7.



Fig. 7: Microwave generated plasma protruding from the cylinder

However, due to the protrusion from the shielding cylinder the electromagnetic radiation increased significantly. Therefore, it was decided to use radio-frequency as excitation source due to the fact that radio-frequency is less dangerous and more easily manageable than microwaves.

3.1.2.2 Radio-frequency (RF) regime

RF-driven plasmas can be divided into capacitively coupled plasmas (CCP or ‘E’-discharges) and inductively coupled plasmas (ICP or ‘H’-discharges). The simplest way to accomplish an ICP is by surrounding the discharge volume with a coil. The changing magnetic field of the RF-current induces an electric field in which the plasma electrons are accelerated. ICPs can achieve electron densities in the range of $n_e = 10^{12} \text{ cm}^{-3}$ [18]. One of the advantages of ICP-discharges is their ability to operate with insulated or external electrodes avoiding reactive processes with metal electrodes. Furthermore, RF-sources can be operated over a wide range of pressure. Typical applications are thin film deposition and plasma etching.

Type ‘E’-discharges are capacitively coupled electrodes carrying a high-frequency signal. The neutral gas between the electrodes acts as a dielectric. The electrodes may be in direct contact with the discharge or can be insulated from it by another dielectric. Electron densities of about $n_e = 10^9 - 10^{10} \text{ cm}^{-3}$ [18] are usual. A specific characteristic of CCPs is the self-biasing, a negative dc potential between the powered electrode and the plasma. In many applications the chamber of the recipient acts as grounded electrode and is therefore larger than the powered electrode. But the currents from the plasma to both electrodes have to be equal. The higher current density at the smaller electrode requires a higher voltage. Hence, the asymmetrical configuration of the electrodes’ surfaces results in a bias voltage.

Above certain frequencies in the Megahertz range the transmission line becomes of comparable dimension to the signal wavelength. Thus, matching networks are necessary in order to match (or tune¹⁰) the output impedance of the generator to the load. A matching network consists of variable capacitances and inductances. Depending on their spatial configuration (connected in series or shunt) they can be divided into ‘L’-type, ‘ π ’-type, and ‘T’-type networks.

If the load is perfectly matched, the generator will work at highest efficiency leading to a maximized power coupled to the load. The term load encompasses everything physically arranged in-line downstream the matching network, i.e. cables, the (vacuum) chamber, and the plasma itself. A mismatch of load impedance to the characteristic impedance Z_0 causes reflected power. A common misconception about power reflection is that the reflected power bounces back to be absorbed by the generator. In fact, reflected power

¹⁰ Tuning implies impedance matching by varying the frequency.

is just the phase shift between the generator's output voltage and output current. Due to this phase shift the generator has to excite additional voltage and current in order to deliver the same load power as in a matched situation. Usually, the output impedance Z of a generator is set to 50Ω which is equal to the characteristic impedance Z_0 of common transmission lines / coaxial cables. A coaxial cable consists of an inner current carrying conductor and a grounded outer conductor acting as return path and shield. Both are separated by a dielectric. In RF-applications the electromagnetic waves propagate in the transverse electric and magnetic mode (TEM). This implies that the electric and magnetic field lines are perpendicular to each other and to the direction of propagation. Like every real element in a circuit, coaxial cables exhibit a certain resistance R' , inductance L' , capacitance C' , and conductance G' per (infinite) unit length. Figure 8 illustrates the schematic of these elementary components of a transmission line.

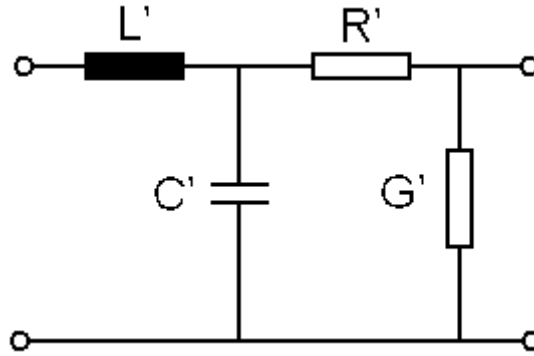


Fig. 8: Equivalent circuitry of a coaxial cable

When R' and G' are negligible small it can be shown that Z_0 is given with

$$Z_0 = \sqrt{\frac{L'}{C'}} \quad (6)$$

Typical values for L' are 125 nH/m and 50 pF/m for C' , respectively. Calculating Z_0 for these values results in:

$$Z_{0(\text{length}=1\text{m})} = \sqrt{\frac{L'}{C'}} = \sqrt{\frac{125 \cdot 10^{-9} \text{ H} \cdot 1 \text{ m}}{50 \cdot 10^{-12} \text{ F} \cdot 1 \text{ m}}} = 50 \Omega \quad (7)$$

Thus, the characteristic impedance Z_0 of a transmission line is *not* dependent on its length but on its internal dimensions.

In order to achieve a matched situation the reactive part X of the load impedance $Z_L = R + jX$ has to be cancelled out by adding its conjugate complex $Z = R - jX$, which is done

by the matching network. It transforms the load impedance to 50Ω . It should be mentioned that the input impedance Z_0 seen by the matching network depends on the cable length between matching network and vacuum chamber. The input impedance Z_{in} of the matching network is given as $Z_{in} = Z_0 \frac{Z_L + jZ_0 \tan(\beta l)}{Z_0 + jZ_L \tan(\beta l)}$ with Z_0 as characteristic impedance, Z_L load impedance, l the cable length and β the imaginary part of the propagation constant. Thus, the electromagnetic waves can travel down the complete transmission line from the generator to the load without experiencing any change of impedance that would cause reflections, similar to an acoustic wave that is partly reflected leading to an echo when it changes the medium.

PART II

4 Experimental procedures and tools

4.1 Experimental setup

Preliminary experiments have been conducted in order to attain a better understanding of the mechanisms and the behaviour of atmospheric pressure plasma devices. The initial device consisted of an approximately 8 cm long stainless steel cylinder with an inner diameter of 10 mm connected to ground. Copper antennas of various diameters were inserted into this cylinder and were supplied with a RF-signal. Helium was inserted to the inter-electrode space. It was observed that the gap due to the different antenna diameters influenced the impedance of the setup significantly. The coaxial configuration acts as a capacitance: decreasing the inner diameter reduces the capacitance, but increases the reactance. Thus, the impedance of the device exceeded the range of the matching network. Using an antenna with a diameter of 8 mm (thereby reducing the gap to 1 mm) enabled the observation of further behavior: the plasma was created in the complete inter-electrode space, but not protruding from the nozzle forming a plume. At higher power filamentary arcs arose. This could be explained with a homogenous electric field distribution between the RF-driven antenna and the ground. The electromagnetic waves at 13.56 MHz¹¹ are more than two orders of magnitude longer than the nozzle itself. Therefore, the potential drop between electrode and ground can be considered equal on the total length. The filamentary arcs arose due to a glow-to-arc transition at higher power. The following conclusions for constructing a new plasma-needle device were drawn from these observations:

- A more or less unipolar electrode-configuration with a protruding antenna and the surrounding acting as ground is necessary to create a plasma plume.
- A sharp electrode tip increases the local electric field and thereby facilitates the plasma ignition.
- The dimensions of the device have to be chosen carefully in order to remain within the range of the matching network and to obtain a non-thermal plasma.
- Shielding of the discharge gas from the electric field prevents undesirable discharges.

¹¹ The wavelength (in vacuum) at 13.56 MHz is $\lambda=22.12$ m.

A valid solution to meet all these requirements was then constructed. The complete experimental setup can be described as follows: The RF-signal was generated by a CesarTM Generator Model 1310 of Advanced Energy which was connected to a Dressler Vario-match VM1000 matching network. The VM1000 had a L-shaped topology consisting of two Comet CVBA-500BC capacitors and a main- and shunt inductor. Unfortunately, the minimum output power of the generator with guaranteed accuracy¹² was limited to 10 W. Unless stated otherwise, all power declarations are delivered power to the load as read off the generator's display, i.e. forward power minus reflected power. RF-power was transmitted to a stainless steel capillary by means of a RG 58 coaxial cable. The outer and inner diameter of the capillary was 1.1 mm and 1.0 mm, respectively. The capillary was surrounded by a dielectric made of polytetrafluoroethylene which itself was surrounded by a stainless steel cladding acting both as ground and as shield. The capillary protruded from the stainless steel cladding by 3.3 mm. All dimensions are visualised in figure 9 and the device is schematically shown in figure 10.

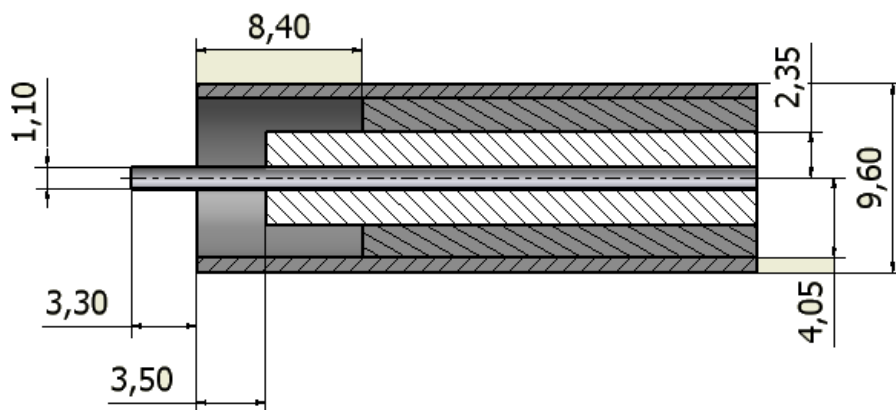


Fig. 9: Schematic sketch of the plasma-needle

This type of device can be used in twofold ways: as a plasma generator for activation and as a coating tool. In the latter case *both* the carrier and reactive gas were inserted to the capillary from the back of the device. For thin film deposition, cyclohexane was added to the discharge gas. The vapour pressure of cyclohexane is given with 104 *hPa* at 20° C.¹³ Therefore, a liquid and a vapour phase coexist in a volume at atmospheric pressure and it was not necessary to heat the liquid cyclohexane in order to increase its vapour pressure.

¹² User Manual CesarTM Generator Model 1310, chapter 3-5.

¹³ Source: <http://de.wikipedia.org/wiki/Cyclohexan>

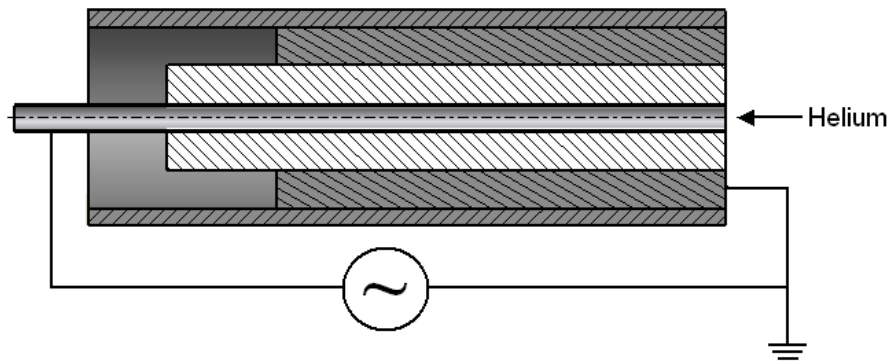


Fig. 10: Schematic sketch of the device and its electrical connection¹⁴

A simple bypass as shown in figure 11 was used to mix the helium with the cyclohexane vapour. Opening and closing the bypass-valve regulated the content of cyclohexane in the mixtures. Within the scope of this work only two different valve positions were used, completely and partly open. The resulting admixtures were calculated in the following chapter.

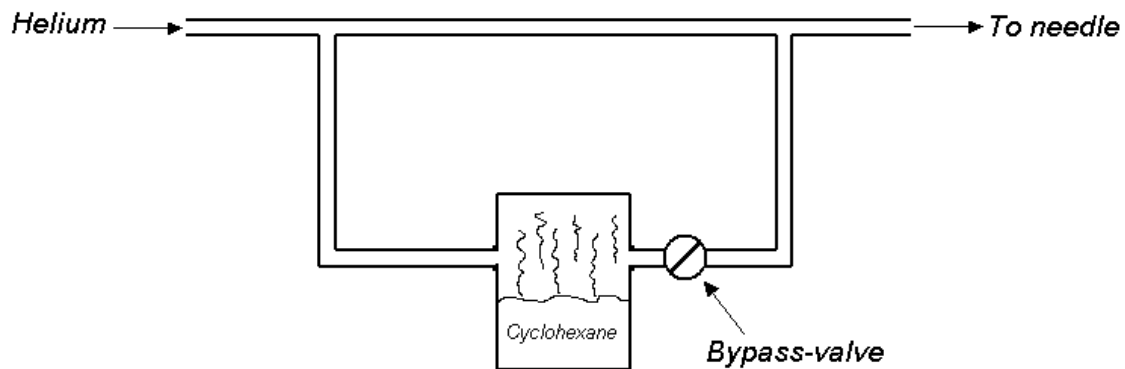


Fig. 11: Schematic of the gas flow

In order to deposit DLC layers, a carbon source is required. Usually, liquid or gaseous hydrocarbons are used. These can be saturated (without double bonds), like methane, ethane, propane, butane, cyclohexane or unsaturated (having double or triple bonds) like ethylene, benzene and acetylene. Besides physical properties they differ in hydrogen-to-carbon ratio, carbon chain length, and hybridization of the carbon atoms. The hydrocarbons are dissociated in the plasma into smaller carbon species which then deposit on the substrate and form a layer. SCHWARZ-SELLINGER ET AL. [19] showed that the precursor gas influences the properties of a deposited thin film. The unsaturated hydrocarbons lead to

¹⁴ Sketches were drawn with Autodesk Inventor Version 9.

films with higher density, lower hydrogen content, and a higher refractive index than saturated hydrocarbons.

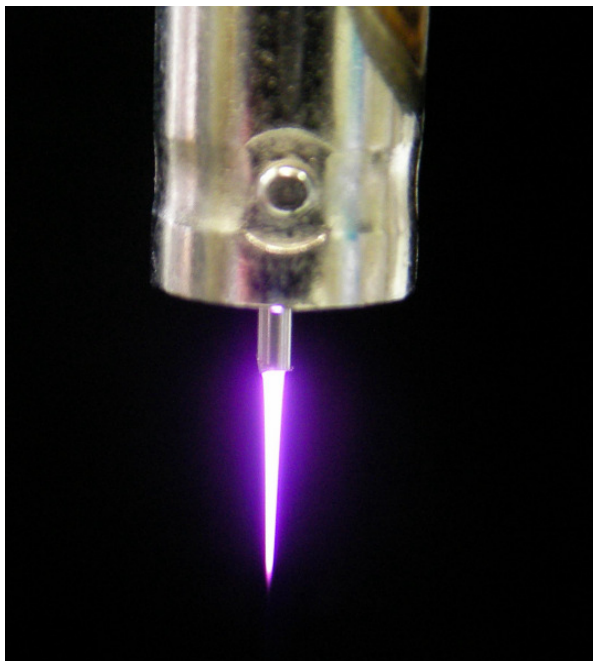


Fig. 12: Pure helium plasma at 25 W

In this work cyclohexane (C_6H_{12}) was used solely as precursor gas. It is comparably easy to handle and does not require many precautions. Depositions were conducted under a fume hood. The admixture of cyclohexane gave rise to a colour change of the plasma plume. It turned from a bright purple (see figure 12) to a pale white-grey (see figure 13). Furthermore, with increasing cyclohexane content the plume size diminished.

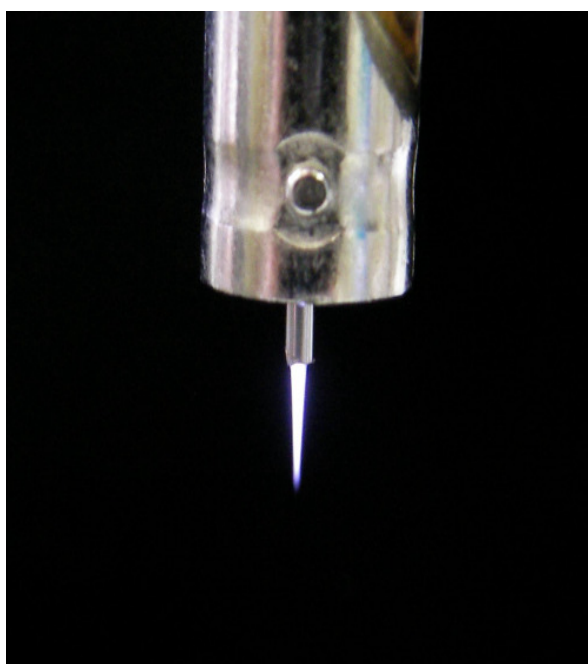


Fig. 13: Helium plasma with admixture of 35 sccm cyclohexane at 25 W

4.1.1 Estimation of the cyclohexane content

In order to estimate the content of cyclohexane in the gas mixture flow, a simple difference measurement was conducted. The mass of the volume containing the liquid cyclohexane was weighted. Afterwards, the plasma was ignited with standard helium flow while the valve of the cyclohexane-bypass was completely opened. Since this method offers only a rough impression of the used cyclohexane, the measurement time was set to one hour to increase accuracy. Afterwards, the volume and the cyclohexane were weighted again. A loss of $m = 7.8 \text{ g}$ was calculated. The difference is due to vaporization of the liquid cyclohexane. Cyclohexane has a molar mass of:

$$M_{\text{Cyclohexane}} = 84.16 \frac{\text{g}}{\text{mole}} \quad (8)$$

The total amount of substance per hour then is:

$$n = \frac{m}{M} = \frac{7.8 \text{ g}}{84.16 \frac{\text{g}}{\text{mole}}} = 0.0927 \text{ mole} \quad (9)$$

The relationship between the amount of a substance given in mol and the quantity of molecules N is given as:

$$N = N_A \cdot n \quad (10)$$

N_A being Avogadro's number, the quantity of cyclohexane molecules in case of a completely opened bypass-valve is $N = 5.582 \cdot 10^{22}$ per hour and $N = 9.303 \cdot 10^{20}$ per minute, respectively.

The volume of one mole of an ideal gas is $V = 22.414 \text{ l}$.¹⁵ Assuming that the vapour of cyclohexane would be an ideal gas, the volume of the above calculated amount of cyclohexane is:

$$V(0.0927 \text{ mole}) = 2.078 \text{ l} \text{ or } 34.63 \text{ sccm} \quad (11)$$

with *sccm* denoting standard cubic centimetre per minute.

The same measurement was conducted a second time with the bypass-valve not completely but partly open just until the content of cyclohexane in the gas mixture gave

¹⁵ Calculated following the ideal gas law $p \cdot V = n \cdot R \cdot T$ with $p = 1.01325 \cdot 10^5 \text{ Pa}$, $T = 273.15 \text{ K}$, and $R = 8.314472 \text{ J} \cdot \text{mol}^{-1} \cdot \text{K}^{-1}$.

rise to a visible change in the colour of the plasma plume. The corresponding calculations are shown in table 3.

Tab. 3: Calculation of cyclohexane content

	Valve completely open	Valve partly open
Mass difference [g]	7.8	1.5
Amount of substance [mole]	0.0927	0.0178
Molecules [h^{-1}]	$5.582 \cdot 10^{22}$	$1.072 \cdot 10^{22}$
Volume [l]	2.078	0.399
Volume [sccm]	34.63	6.65

Since the content of cyclohexane is depending on both the overall helium flow – which is unknown – and the opening of the bypass-valve, these results can only be considered as rough calculations. Furthermore, in case of the partly opened valve there is no precise repeatability given. Thus, the content of cyclohexane in the gas mixture was considered as 35 sccm and 7 sccm, respectively.

4.2 Plasma diagnostics

4.2.1 Voltage and current measurements

Besides non-invasive spectroscopic techniques, the measurement of voltage and current offers the possibility to characterize the plasma properties, mainly the plasma impedance and the coupled power. The power P is given as:

$$P = \frac{1}{T} \int_0^T U(t) \cdot I(t) \quad (12)$$

with U being the voltage, I the current and T the oscillation period. Furthermore, having the phase difference between voltage and current, the impedance Z can be calculated. The impedance Z consists of a resistive and a reactive part.

The reactive part of the impedance can consist of an inductance L and a capacitance C which are both dependent on frequency f .

$$Z = R + j\left(\omega L - \frac{1}{\omega C}\right) \quad (13)$$

Additionally, one can obtain information about the breakdown voltage, i.e. the voltage necessary for plasma ignition. In contrast to Langmuir probes, which will be presented in the subsequent chapter, the current and voltage probes are not immersed into the plasma, but connected only to the transmission line. Due to the power dissipation of the matching network and the transmission lines, which are placed in line between the generator and the load, the power measurement of the RF-generator is not reliable. Therefore, a self-made power meter was connected between the matching network and the load being the capillary (see figure 14) [cp. 20].

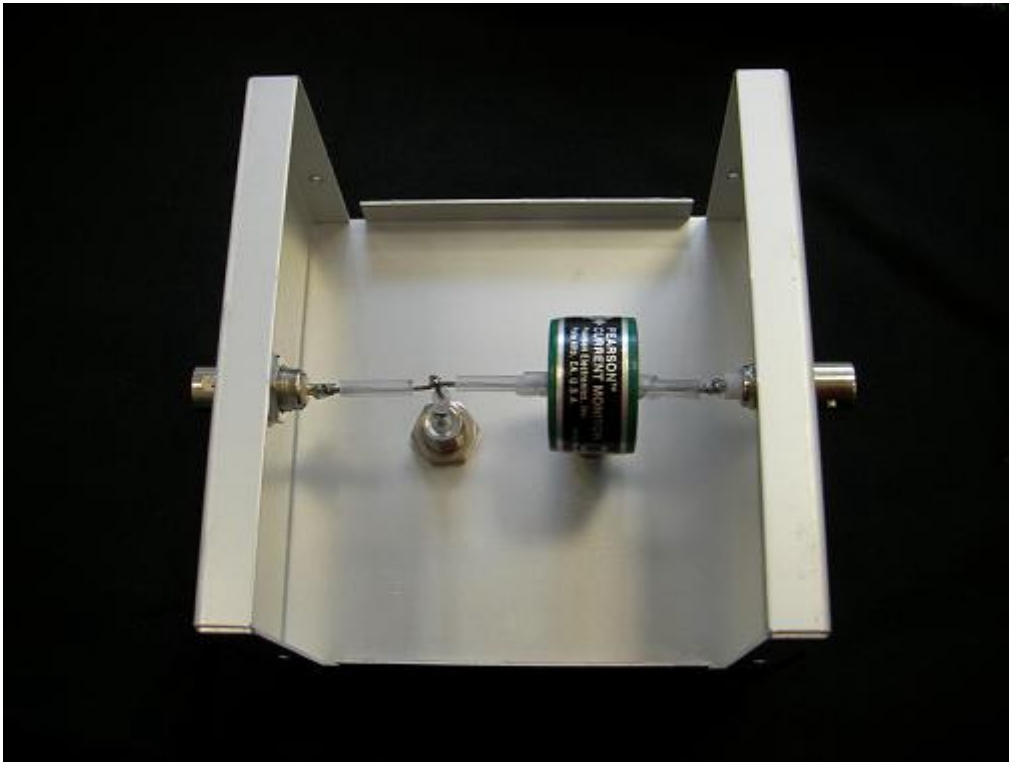


Fig. 14: Self-made power meter

The power meter was positioned between the matching network and the load. It consisted of a PearsonTM Current Monitor Model 2877 from Pearson Electronics, Inc. and a passive high voltage probe P5100 from Tektronix. Both probes were connected via 50 Ω coaxial cables to a LeCroy 9314M oscilloscope. Preliminary experiments revealed that a high voltage probe with an attenuation factor of 100 is required in this case. The current monitor is basically a Rogowski coil¹⁶. The outer conductor of the coaxial cable whose current was to be measured was stripped and the conductor was aligned in the centre of the coil. The voltage induced in the coil is proportional to the current in the conductor. Since

the coil has an air core, the inductance of the probe was negligible. The rise time was 2 ns as provided by the manufacturer. The P5100 has an attenuation factor of 100 and a circuit loading of $R_{PR} = 10\text{ M}\Omega$ and $C_{PR} < 2.75\text{ pF}$. The circuit loading of the voltage probe is strongly dependent on the frequency. The probe can be represented by a resistance mounted in parallel with a capacitance as depicted in figure 15.

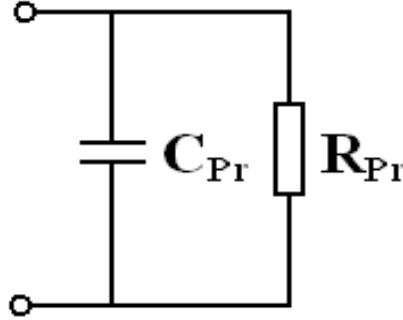


Fig. 15: Schematic of the voltage probe

The probe impedance is then given as:

$$Z_{PR} = \frac{1}{j\omega \cdot C_{PR} + \frac{1}{R_{PR}}} \quad (14)$$

This can be written in the Laplace domain with $s = j\omega$ as:

$$Z_{PR}(s) = \frac{R_{PR}}{\tau_{PR} \cdot s + 1} \quad (15)$$

with the time constant

$$\tau_{PR} = R_{PR} \cdot C_{PR} = 10 \cdot 10^6 \frac{\text{V}}{\text{A}} \cdot 2.75 \cdot 10^{-12} \frac{\text{As}}{\text{V}} = 27.5 \cdot 10^{-6} \text{ s} . \quad (16)$$

The phase angle ρ_{PR} of the probe is given as:

$$\rho_{PR} = \arctan\left(\frac{\text{Im}(Z_{PR})}{\text{Re}(Z_{PR})}\right) = \arctan(-\tau_{PR} \cdot \omega) \quad (17)$$

At 13.56 MHz ($\omega = 85.2 \cdot 10^6 \text{ s}^{-1}$), the $|Z_{PR}|$ is reduced from its dc value of 10 M Ω to

$$|Z_{PR}(s)| = 4266 \Omega \quad (18)$$

¹⁶ Named after its inventor Walter Rogowski. Electrical device for measuring alternating current based on mutual inductance.

This reduced small impedance value implies that the voltage probe is affecting the electric circuit and therefore must be taken into account for further calculations.

4.2.1.1 Probe calibration

The measured phase shift between voltage and current was falsified. The cables which connected the current and voltage probe to the oscilloscope had different lengths. The cable length of the voltage probe was 3.1 m, the one of the current probe 1 m. This difference induces a time delay. This signal delay is dependent on the frequency and the cable length difference. The phase shift resulting from this error can be calculated as:

$$\Delta\rho = 360^\circ \cdot f \cdot \Delta t \quad (19)$$

with f denoting the frequency and Δt the signal delay, which itself can be calculated as

$$\Delta t = \frac{\Delta l}{c} \quad (20)$$

with Δl denoting the difference in cable lengths and c the speed of light. This results in a phase shift of 16.27° at 13.56 MHz per meter cable difference. This resulted in a necessary correction of the phase shift of:

$$\Delta\rho = (-2.1\text{ m}) \cdot 16.27 \frac{\text{deg}}{\text{m}} \approx (-34.2^\circ) \quad (21)$$

The complete electric circuitry consisting of the RF-generator, the matching network, the plasma-needle and the voltage probe is shown in figure 16. The matching network is represented by its load-capacitor and –inductor C_L and L_L and its tune-capacitor and –inductor C_T and L_T , respectively. C_N and R_N represent the impedance of the needle consisting of a resistive and capacitive part. The attachment of the voltage probe adds considerable impedance to the circuitry. Therefore, its impedance was taken into account in terms of the capacitance C_{Pr} and R_{Pr} . To simplify this model, it was assumed that the ground lead of the voltage probe has a negligible inductance. The self-made power meter was connected to the circuitry and the altered load impedance was compensated by the matching network.

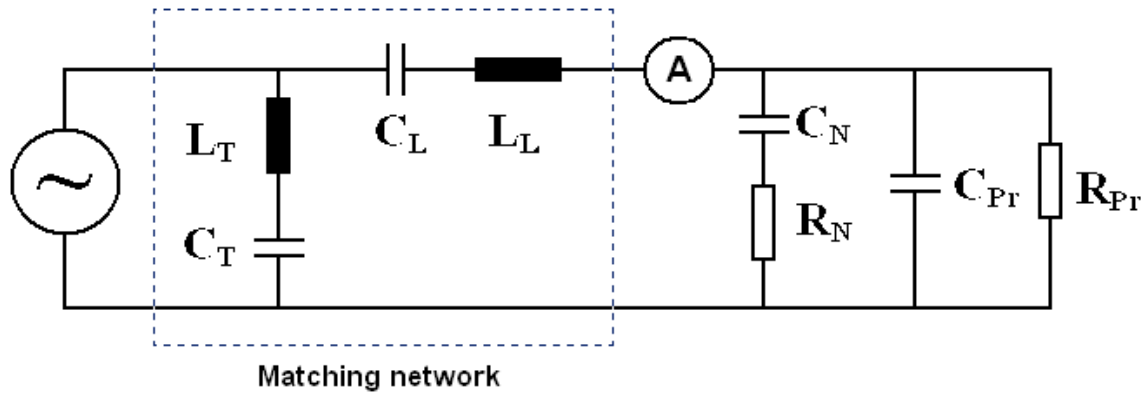


Fig. 16: Schematic of the electric circuitry with attached voltage probe

4.2.2 Langmuir probes

Although Langmuir probes are of inestimable aid for characterizing low pressure plasmas, they are less helpful in case of atmospheric pressure plasmas. Langmuir probes are common diagnostic tools to obtain information about electron density, ion density, floating potential, plasma potential and electron temperature. In principle, a Langmuir probe consists of a conductor which is connected to a variable-voltage supply that is inserted into the plasma. As soon as this conductor is suspended in the plasma it will be struck by electrons and ions with charge fluxes. As a result of the higher velocity and lower mass of the electrons, the electron flux is much larger than the ion flux. Therefore, if the conductor is isolated, it immediately starts to build a negative charge, or in other words, a negative potential with respect to the plasma. This potential is called floating potential Φ_{fl} . The potential of the undisturbed plasmas is termed plasma potential Φ_{pl} . Dependent on the potential difference between probe and plasma that can be manipulated by the voltage-supply, charge carriers are attracted to (or repelled from) the probe resulting in an electric current. This resulting current is dependent on the geometry of the probe and the plasma density, potential and temperatures. A typical Langmuir probe characteristic is shown in figure 17. It can be divided into three parts which are separated by the above mentioned floating- and the plasma potential Φ_{fl} and Φ_{pl} . If the probe is biased very negatively with respect to the plasma potential, the electric field around the probe prevents electrons from reaching the probe. The current collected by the probe is then only due to positive ions, thus it is called ion-saturation current I_{is} . Increasing the probe potential enables more and more electrons to overcome the electric field and contribute to the current. The floating potential is given for $I(\Phi_{fl}) = 0$. At this voltage the currents of positive and negative particles on the probe are equal.

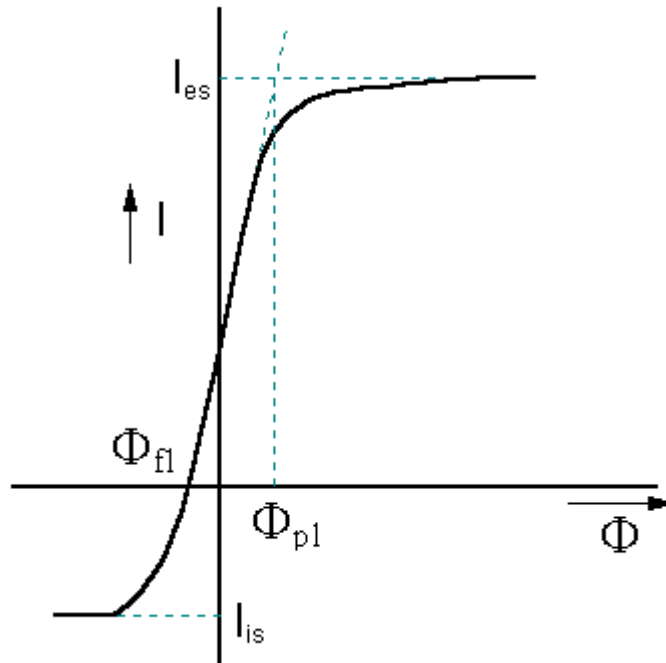


Fig. 17: Typical Langmuir probe characteristic

If probe and plasma potential are equal, there is no electric field between the probe and the plasma. The particle collection at the probe then occurs only due to the thermal velocity of the particles. Since the electron thermal velocity is greater than that of ions the collected current is mainly due to electrons. This current is termed electron-saturation current I_{es} . Between the ion- and electron saturation one can find the retarding field which gives information about the energy distribution of the electrons [21].

Experiments were executed with a self-made Langmuir-probe system. The obtained results were not comparable to typical characteristics as presented above and did not allow any reasonable calculation of plasma properties.

Unfortunately, the basic assumptions that underlie the interpretation of Langmuir-probe characteristics become critical at atmospheric pressure [22]. Furthermore, – in contrast to DC-discharges – the plasma potential in RF-excited plasmas is varying over time, influencing the measurement and leading to a wrong plasma potential interpretation [23]. Basically, there are two methods to overcome this problem, active and passive RF-compensation. Active compensation works with an externally generated signal matched in phase and amplitude which is superposed to the probe's RF-signal. Passive compensation denotes filtering of RF-distortions by means of band filters [24]. Finally, invasive methods are rather inappropriate for small-sized plasmas since every invasion disturbs the plasma and thereby influences the measurement.

4.2.3 Optical emission spectroscopy

The optical emission spectroscopy (OES) is a non-invasive diagnostic method that allows the investigation of atoms, ions and molecules within a plasma. It is a widely used diagnostic tool for the analysis of plasmas and even more valuable for the characterization of small-sized plasmas since those plasmas are very sensitive to invasive diagnostics. The use of OES in the diagnosis of low density, low temperature plasmas has been ubiquitous and has yielded a lot of information about the properties of materials within the plasma. As mentioned in chapter 3.1.1, the energy difference between an excited- and a ground state atom in a plasma is transformed by an emission of a photon. The dependence between the energy of the photon and its frequency is given with:

$$\Delta E = E_e - E_g = h \cdot f \quad (22)$$

The corresponding wavelength λ can be derived from the frequency as:

$$\lambda = \frac{c}{f} \quad (23)$$

The obtained spectra allow the classification of the atoms and molecules present in the plasma. The spectra of samples containing many elements can be very congested, and spectral separation of nearby atomic transitions requires a high-resolution spectrometer. The incoming light is divided into wavelengths by means of a monochromator and subsequently detected and transformed into an electric signal. There are several methods for detecting the emission, namely photomultiplier tubes (PMT) and detectors based on semiconductors as charge coupled devices (CCD), charge injection devices (CID) or photodiode arrays (PDA). All four systems are based on the photoelectric effect. In a photomultiplier tube, electrons are relieved from the surface and emitted due the incoming photons. This is termed photoemission. Semiconductor-based detectors take advantage of the inner photoelectric effect: electrons are excited to the conduction band of the semiconductor.

4.3 Surface modification experiments

4.3.1 Contact angle measurements

Contact angle measurements offer an easy possibility to determine surface energy, i.e. whether a surface has a hydrophobic or a hydrophilic character. Surface energy is the combination of non-polar and polar energy. Non-polar energy exists between all mole-

cules, whereas polar energy exists only when polar groups are present. Therefore, a surface treatment with a plasma containing polar groups (for example OH) can increase the surface energy and make the surface more hydrophilic, whereas, for example, a plasma-deposited fluorinated DLC-film is one possibility if a more hydrophobic surface is desired.

Surface energy is always positive since energy is required for the disruption of chemical bonds. Thermodynamically, the most stable steady state of a system is the one containing the lowest energy. Thus, each system has the ambition to avoid surfaces with high surface energy or to minimize them. From this it follows, that materials with high surface energy are easily wetted by materials which have lower surface energy, but not conversely. Water has high surface energy by nature; it is polar and forms hydrogen bonds. Depending on the surface energy of its counterpart water will wet a surface or not and therefore, surface energy is in the majority of cases quantified using contact angle measurements: a droplet of (deionized) water is poured on the substrate. The three different phases balance at thermodynamic equilibrium at the edge of that drop. Denoting the solid-liquid energy as E_{SL} , the vapour-liquid energy as E_{VL} , and the vapour-solid energy as E_{VS} , the interfacial energies satisfy the following (known as Young's) equation in equilibrium:

$$E_{SL} + \cos \theta \cdot E_{VL} = E_{VS} \quad (24)$$

The angle θ is measured as presented in figure 18.

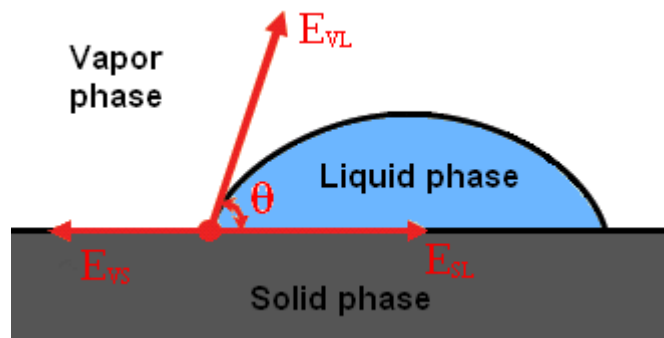


Fig. 18: Droplet on a surface forming a contact angle

The higher the surface energy of the solid, the lower is the contact angle. Surfaces exhibiting contact angles between 10° to 30° are considered as hydrophilic, whereas contact angles between 70° to 90° are awarded to hydrophobic surfaces. Furthermore, there are surfaces on which water droplets form contact angles almost up to 180° . These surfaces are termed superhydrophobic. A typical example is the leaf of the Lotus flower. Their super-

hydrophobicity is due to little protuberances giving rise to a rough surface. Hence, the hydrophobicity of surfaces is affected not only by the chemical composition but also by their roughness.

4.3.2 Enzyme-linked immunosorbent assays (ELISA)

As mentioned in the introduction plasma treatment can be used to improve protein binding on culture substrates. One example for those culture substrates are microtiter plates for Enzyme-Linked Immunosorbent Assays (ELISA). ELISA are common biochemical diagnostic tools for detecting proteins, viruses, hormones, toxins or pesticides in a sample. The idea of an ELISA is based on the specific bonding of antibodies for a particular antigen. In simple terms, an unknown amount of antigen in a sample is immobilized on a surface. This can be done either with physical or chemical methods. Normally, this is done non-specifically via adsorption to the surface which is a physical method. The advantage of this approach is its simplicity, since no additional chemicals are required. The major disadvantage is the weak interaction between the surface and the molecule giving rise to low chemical and physical stability. A particular antibody is washed over the surface that then bonds to the antigen. This antibody is linked to an enzyme. Adding a chemical, which is converted by an enzymatic reaction to a light signal, allows the quantification of the antigen.

An improved adhesion between the antigen and the surface of the microtiter plate could increase the threshold and thereby reduce the amount of necessary antigen. Thus, a microtiter plate was treated with the plasma-needle as shown in figure 19. Afterwards, an ELISA was conducted. The microtiter plate was incubated overnight at 4 °C with immunoglobulin *G* (IgG) – containing phosphate buffered saline (PBS), a common buffer solution in biochemistry. The parent solution was diluted in order to obtain different IgG-concentrations for the different rows on the microtiter plate. Subsequently, the standard procedure of an ELISA was conducted, i.e. manifold rinsing, blocking, and incubating for 30 minutes with – in this case – Avidin-peroxidase (Sigma Aldrich A3151). Finally, hydrogen peroxide and ABTS¹⁷ as co-substrate were added and the absorbance at 405 nm was measured twenty minutes later. The peroxidase which is bound to the IgG catalyzes the reaction of the hydrogen peroxide with ABTS:

¹⁷ ABTS refers to 2,2'-azino-bis(3-ethylbenzthiazoline-6-sulphonic acid, a co-substrate with H₂O₂.



The oxidized form $ABTS^+$ is green and has an absorbance maximum at 405 nm which can be detected with a spectrophotometer. Thus, the more IgG is attached to the wells, the more Avidin-peroxidase can be bound. The more peroxidase is bound, the more ABTS can be converted to $ABTS^+$ and the higher is the measured absorbance.

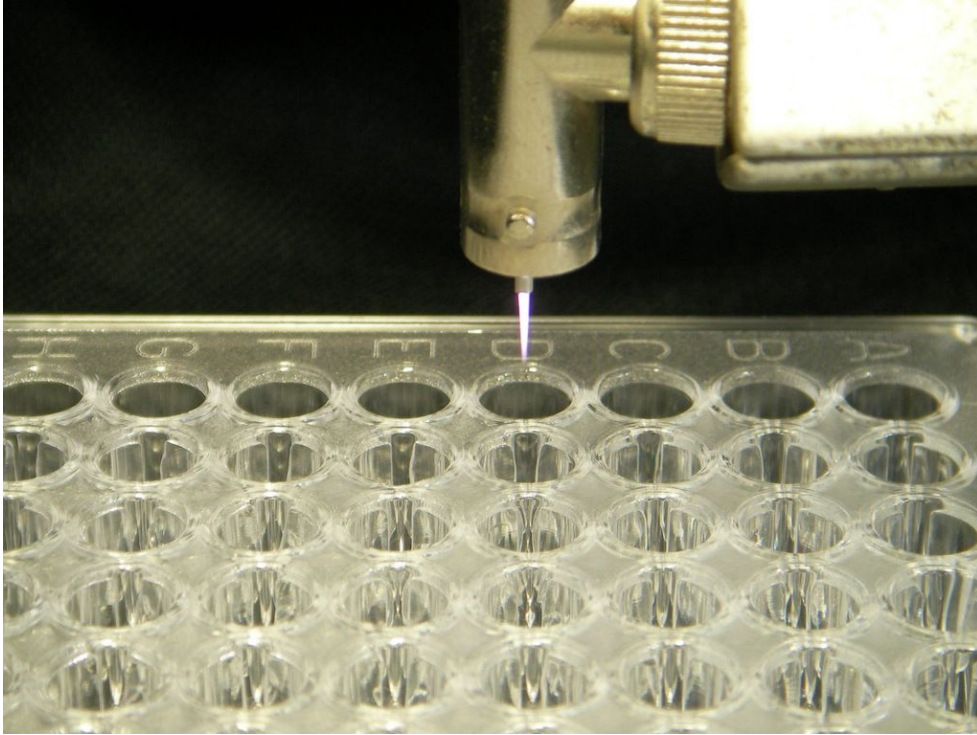


Fig. 19: Plasma treatment of microtiter plate

4.4 Carbon film deposition

4.4.1 Profilometry

There are several methods to determine the thickness of a deposited film. On the one hand there are optical methods, like ellipsometry and interferometry, on the other hand there are mechanical procedures, like profilometry. In this work, thickness has been measured with profilometry. The profilometer (Dektak8 Advanced Development) takes measurements electromechanically by moving a diamond- or silicon-tipped stylus over the sample. The gantry moves the stylus according to the programmed scan length, speed and stylus force. As the scan drive moves the stage and sample, the stylus rides over the sample surface. Surface variations cause the stylus to be translated vertically. Electrical analog signals corresponding to the stylus' movement are produced, which are converted to a digi-

tal format through an analog-to-digital converter. The digitized signals are processed by the software that visualizes the results as two- or three dimensional plots.

Common applications of such profilometers are found in the semiconductor industry, for example for thickness and roughness characterization of thin- and thick-film coatings or wafers, stress calculations in thin films or measurement of etch and trench depths. Optional super-sharp styli with radii down to $0.2\ \mu\text{m}$ allow measurements which require high horizontal resolution of soft films. Stylus forces down to an equivalent of $0.03\ \text{mg}$ offer scratch-free measurements. The stylus that was applied in this work has a radius of $5\ \mu\text{m}$, the stylus force was set to $3\ \text{mg}$. Figure 20 shows the stage of the profilometer.



Fig. 20: Sample loaded on profilometer

4.4.2 Fourier transform infrared spectroscopy (FTIR)

Fourier Transform Infrared Spectroscopy (FTIR) is a powerful tool for identifying types of chemical bonds in a molecule by producing an infrared absorption spectrum. By interpreting that infrared absorption spectrum, the chemical bonds in a molecule can be determined. Both organic and inorganic chemicals can be identified with FTIR. While organic compounds have very rich, detailed spectra, inorganic compounds are usually much simpler. Examples¹⁸ of such spectra are presented in figure 21 for lead nitrate and glycer-

¹⁸ Source: <http://webbook.nist.gov/cgi/cbook.cgi?ID=B6000533&Units=SI&Mask=80#IR-Spec> and <http://webbook.nist.gov/cgi/cbook.cgi?ID=C56815&Units=SI&Type=IR-SPEC&Index=1#IR-SPEC>

ine.

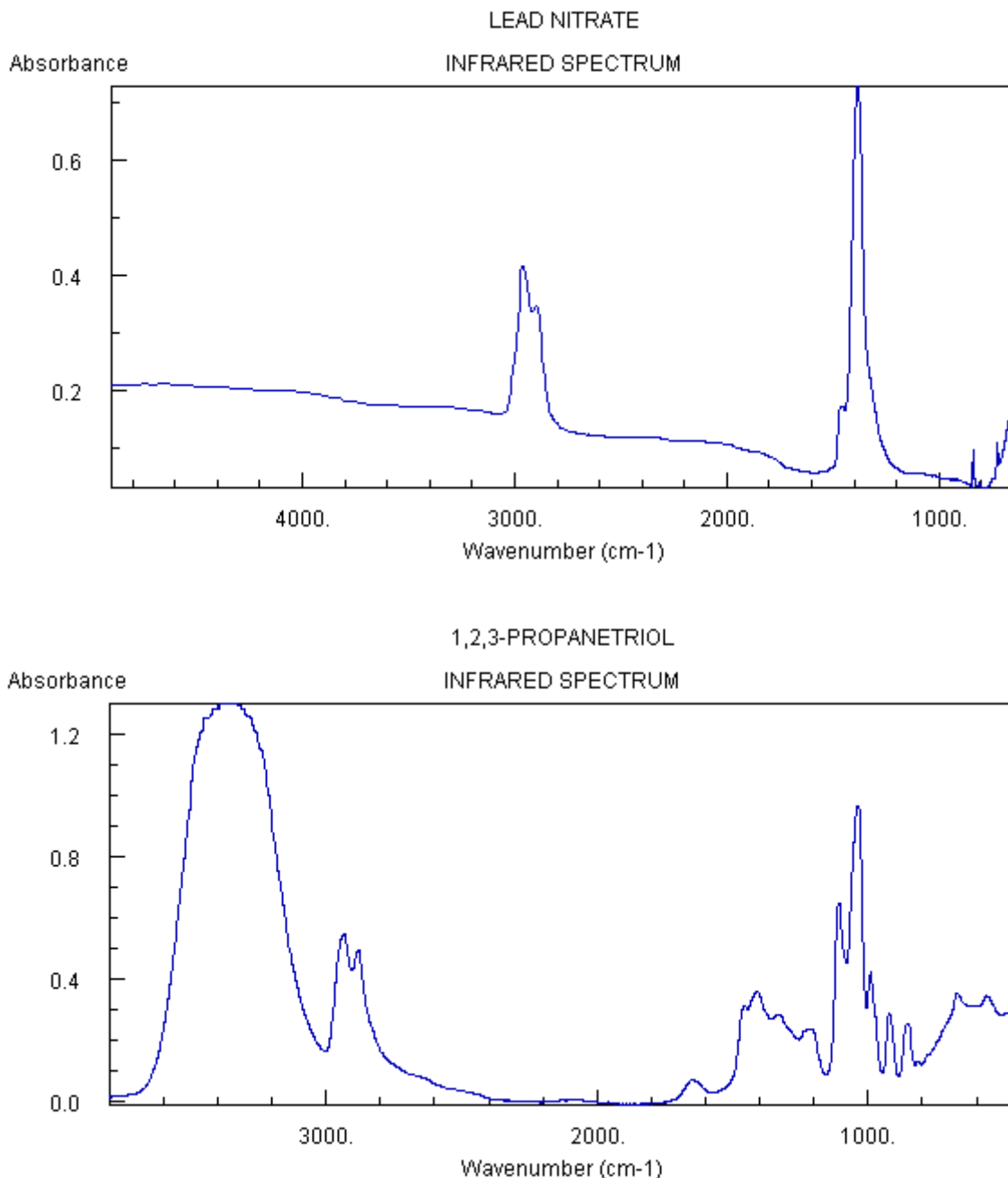


Fig. 21: Typical FTIR spectra of lead nitrate (upper) and glycerine (lower)

Pure compounds normally reveal such unique FTIR spectra, like molecular fingerprints. Furthermore, since the intensity of the absorption is proportional to the concentration of the molecule FTIR can be used for quantitative analyses in unknown mixtures. The analysis of solids, liquids, and gases is possible.

The vibration of molecular bonds depends on the elements forming the bond on the type of bond. For any given bond, there are several specific frequencies at which it can vibrate. These frequencies correspond to the ground state at the lowest frequency and sev-

eral excited states at higher frequencies. The absorption of light energy results in an increased molecular vibration. For any given transition between two states, the light energy, which is determined by the wavelength, must exactly equal the difference in the energy between the ground state E_0 and the excited state E_1 :

$$E_1 - E_0 = h \cdot \frac{c}{l} \quad (26)$$

with h denoting the Planck' quantum, c the speed of light, and l the wavelength of light. FTIR has some advantages over common infrared spectroscopy. In contrast to the latter, each data point of the interferogram contains information about the complete spectrum and the *amount* of data points is affecting the *resolution* of the spectrum. This is called Fellgett- or multiplex advantage. Furthermore, no slit in the apparatus reduces the intensity of the beam. Assuming that the optical losses due to the mirrors and the lenses is negligible, an interferometer's output will be nearly equal in intensity to the input intensity, thus enabling an easier detection of the signal and improvement of the signal-to-noise ratio (Jacquinot advantage).

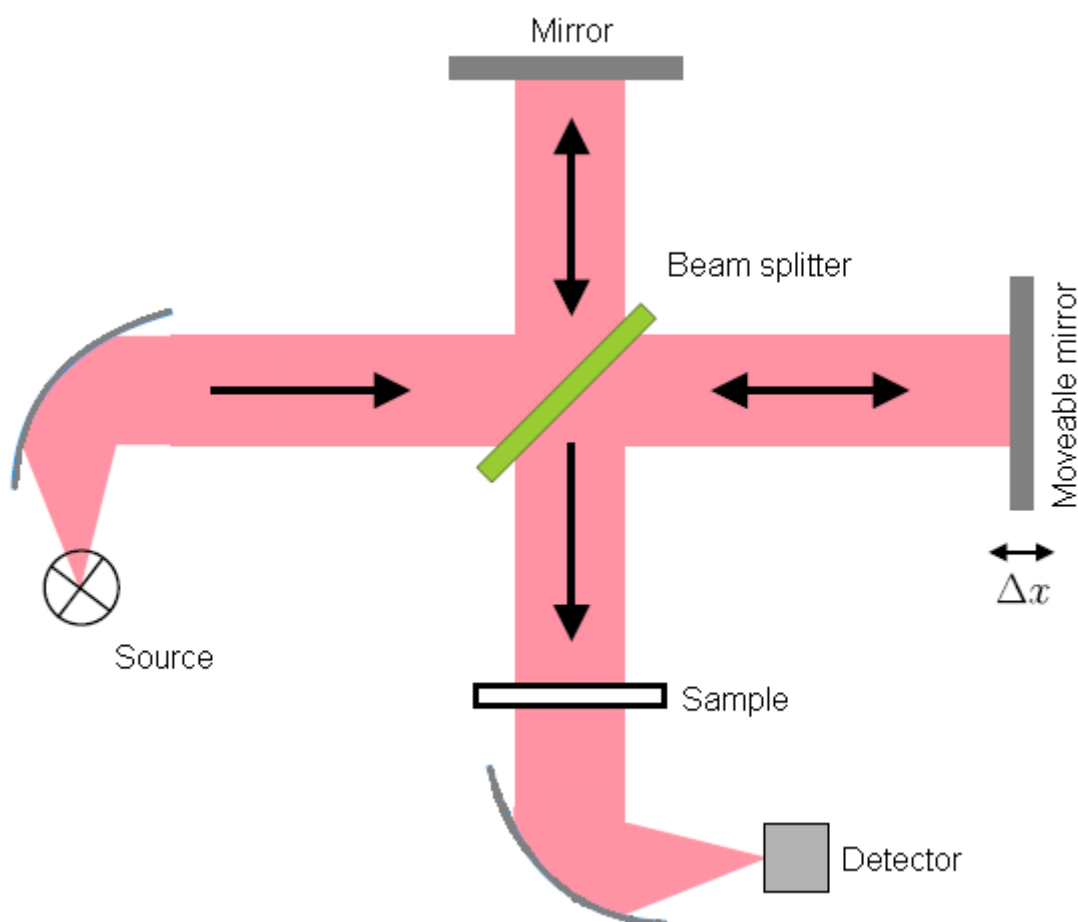


Fig. 22: Schematic illustration of an FTIR spectrometer

A schematic setup of an interferometer is presented in figure 22. The light beam from the source is split into two beams of equal intensity. One beam is directed to a fixed mirror and acts as reference, whereas the other is directed to a moving mirror, which introduces a time delay. Both beams are recombined afterwards and interfere. If the distance Δx of the optical path is equal or a multiple of the wavelength λ ($\Delta x = n \cdot \lambda$ with $n = 0, 1, 2, \dots$), the beams interfere constructively as exemplified in figure 23.

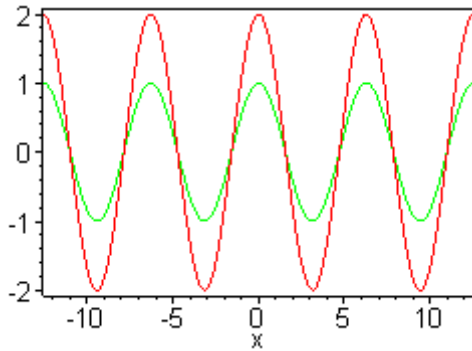


Fig. 23: Constructive interference of two beams

The superposition of two beams for a distance Δx different than a multiple or a half wavelength is presented in figure 24.

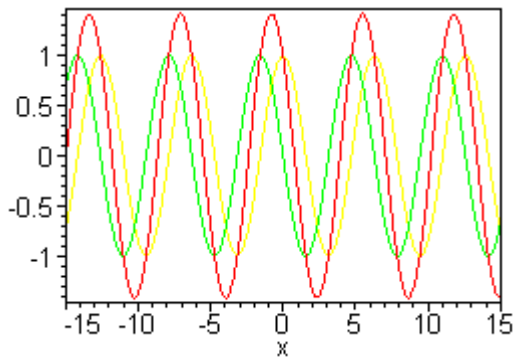


Fig. 24: Superposition of two beams

If the distance differs half a wavelength ($\Delta x = (2 \cdot n + 1) \cdot \frac{\lambda}{2}$), the beams interfere destructively (see figure 25).

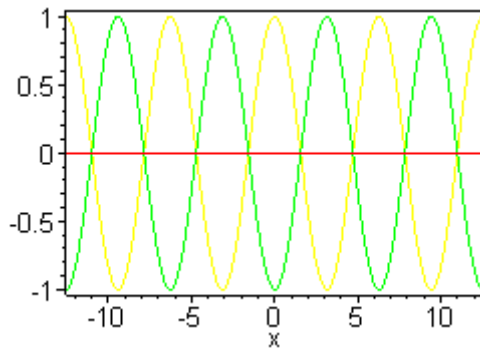


Fig. 25: Destructive interference of two beams

Figure 26 depicts three light beams of different wavelengths, that are in phase for $\Delta x = 0$.

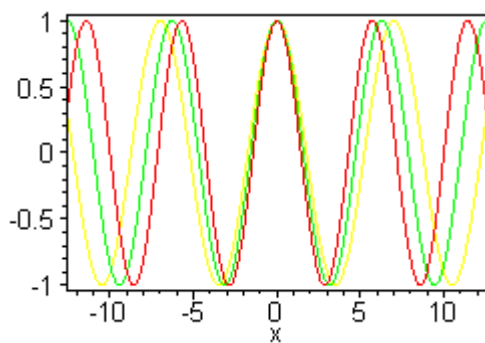


Fig. 26: Three light beams of different wavelength

Since the light source is emitting polychromatic light, the described interference exists for every wavelength. Correspondingly, the intensities of all different interferences superpose. This is exemplified in figure 27 for three different wavelengths.

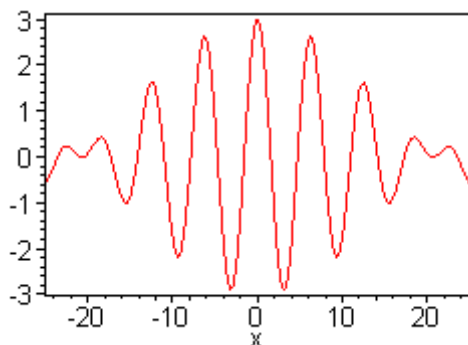


Fig. 27: Superposition of three light beams

One can find the maximum for $x = 0$ at which all three waves are in phase. If the interferogram of the complete spectrum is recorded, this so-called centerburst is even more

evident. When the interferogram signal is transmitted through or reflected by the sample surface, the specific frequencies of energy are absorbed by the sample due to the excited vibration of functional groups in the molecules. Thus, the signal measured by the detector is *not* the absorption spectrum but the IR-intensity as a function of the discrete position of the mirror. Hence, the absorption spectrum (in the frequency domain) can be calculated from this interferogram (in the time domain) using Fourier transform. The results can also be given as transmittance spectra. The dependence between absorption A and transmittance T is $A = -\log_{10}(T)$.

5 Results and discussion

5.1 Characterization of the plasma-needle

5.1.1 Electrical measurements

5.1.1.1 Breakdown voltage and U-I characteristic

The breakdown voltage, i.e. the voltage required for plasma ignition was measured for a pure helium plasma and a helium plasma with an admixture of 7 sccm cyclohexane by stepwise increasing of the voltage. In both cases the ignition occurred at similar values: 274 V_{pk-to-0} for the helium plasma and 272 V_{pk-to-0} for the mixture, respectively. These values are comparable to the ones presented by STOFFELS ET AL. [1].

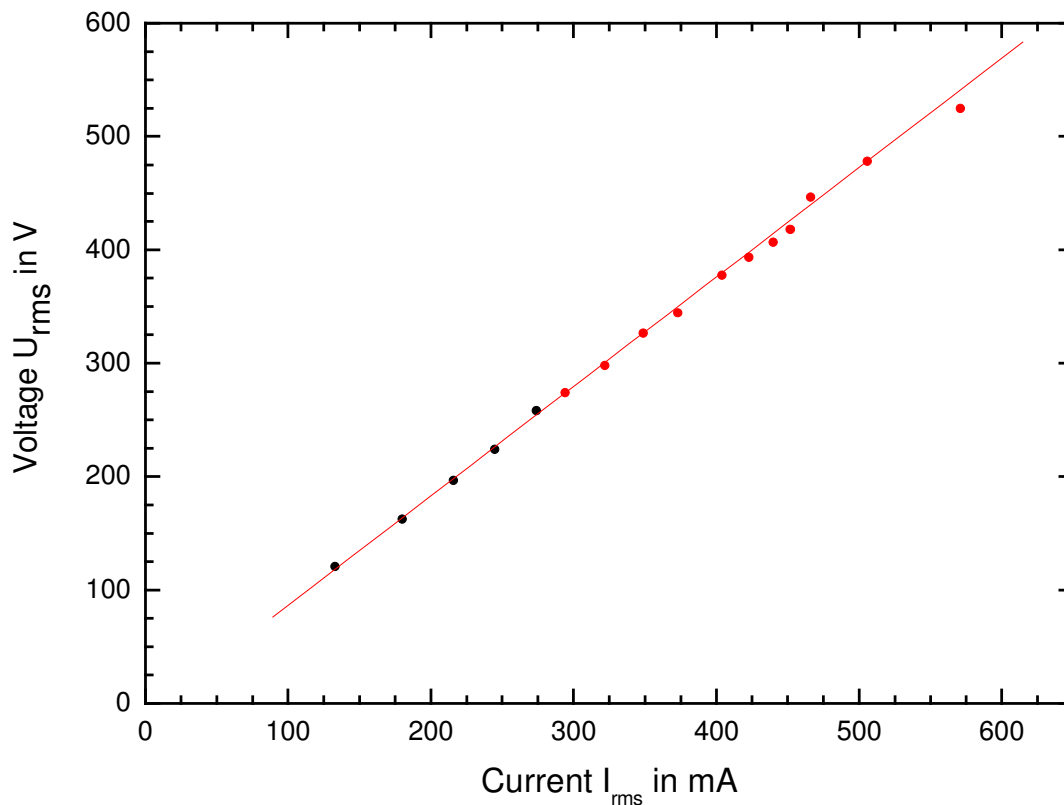


Fig. 28: U-I characteristic of the plasma-needle device for a pure helium plasma

The linear dependence between current and voltage is presented in figure 28. The colour change of the dots marks the presence of plasma. With increasing current the voltage increased as well. Thus, the resistive part of the system's impedance did not change.

5.1.1.2 Determination of the resistive power dissipation

Figure 29 presents measured waveforms of the current and voltage signal for a pure helium plasma. The slight distortion of the sinusoidal signals is due to the oscilloscope's comparably low sample rate of 100 Megasamples per second which corresponds to a sampling period of 0.1 ns.

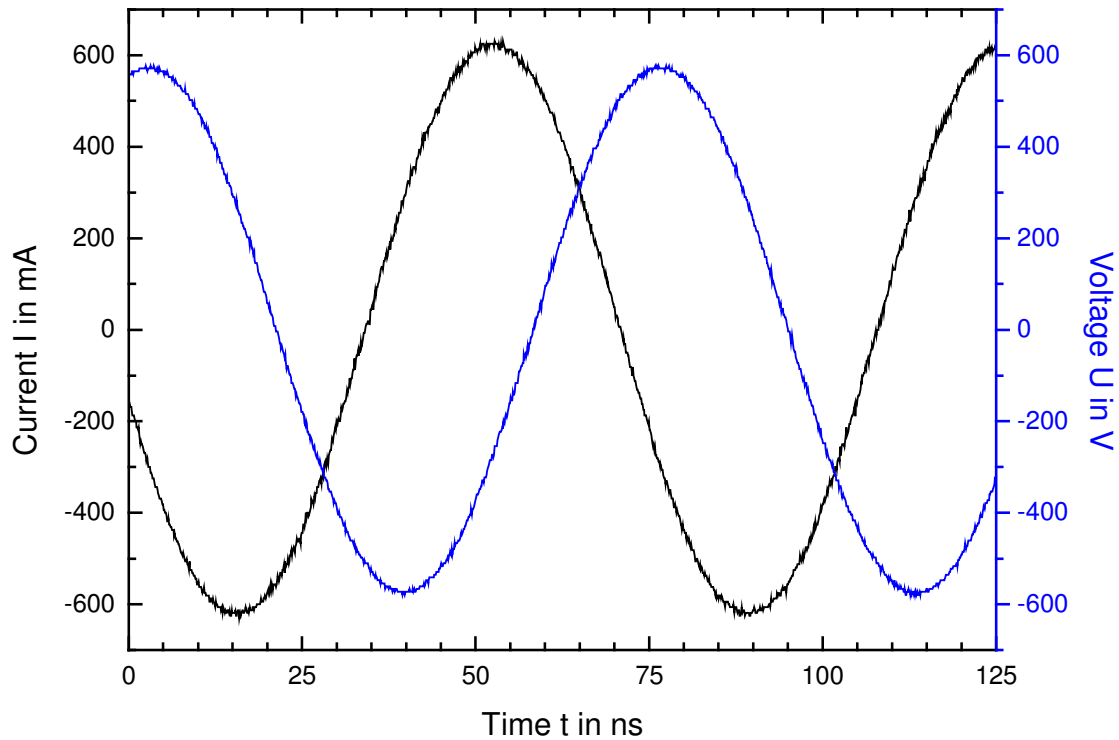


Fig. 29: Typical measured waveforms

In order to facilitate the peak determination, the results were smoothed and peaks were selected as shown in figure 30.

Table 4 lists the results of the peak determination of voltage and current, and the measured phase angle. The measured phase angle of -119.1° appears to be not realistic. By subtraction of the phase angle induced by the probe cable length, one obtains the corrected phase angle $\rho_{\text{corr.}}$:

$$\rho_{\text{corr.}} = \rho - (-34.2^\circ) = (-119.1^\circ) - (-34.2^\circ) = (-84.9^\circ) \quad (27)$$

This high value reflects the capacitive nature of the plasma-needle.

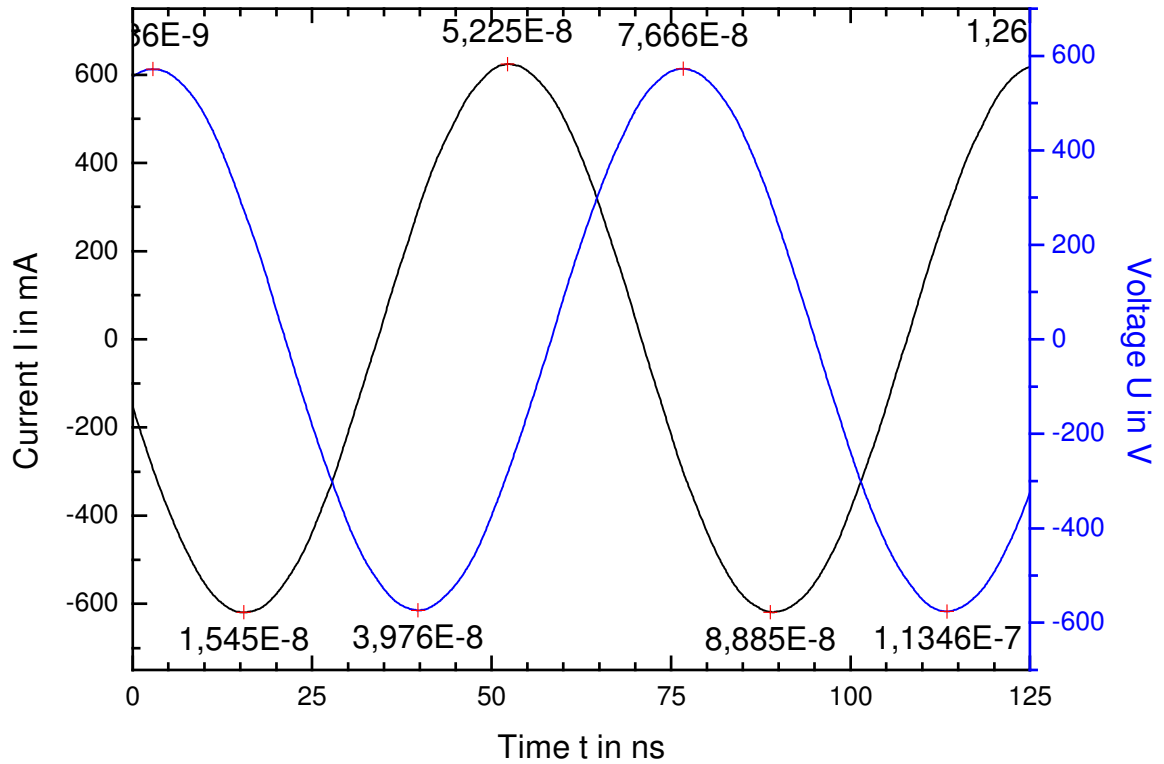


Fig. 30: Current and voltage signals after smoothing and peak determination

Tab. 4: Peak voltage, peak current, and phase shift

	Abs. value voltage in V	Abs. value current in A	Δt in ns	ρ	$\rho_{corr.}$
I	573.7	0.619	-24.3	-118.6°	-84.4°
II	573.1	0.624	-24.4	-119.1°	-84.9°
III	576.0	0.619	-24.6	-120.1°	-85.9°
Mean	574.3	0.621	-24.4	-119.1°	-84.9°

Having voltage, current, and the corrected phase angle, one can calculate the power P dissipated in the system:

$$P = V_{rms} \cdot I_{rms} \cdot \cos(\rho_{corr.}) = 406.1V \cdot 0.439A \cdot \cos(-84.9^\circ) = 15.8W \quad (28)$$

Furthermore, the impedance of the probe-needle system can be calculated as follows:

$$Z_{Pr+N} = U_{rms} / I_{rms} = 925.1 \Omega. \quad (29)$$

These calculated power and impedance values were obtained for the complete system. However, the consumed power in the plasma is of greater interest. V. LÉVEILLÉ AND S. COULOMBE [25] have presented a stepwise approach for this problem. By solving the following two equations, the impedance of the needle consisting of a resistive part R_N and a capacitive part C_N can be calculated.

$$Z_{Pr+N}(s) = R_{Pr} \frac{\tau_N \cdot s + 1}{(\tau_{Pr} \cdot \tau_N) \cdot s^2 + (\tau_{Pr} + \tau_N + R_{Pr} \cdot C_N) \cdot s + 1} \quad (30)$$

$$\rho_{Pr+N} = \arctan\left(\frac{\text{Im}(Z_{Pr+N})}{\text{Re}(Z_{Pr+N})}\right) = \arctan\left(\frac{R_{Pr} \tau_N \omega(1 - \tau_{Pr} \tau_N \omega^2) - R_{Pr} (\tau_{Pr} + \tau_N + R_{Pr} C_N) \omega}{R_{Pr} \tau_N \omega^2 (\tau_{Pr} + \tau_N + R_{Pr} C_N) + R_{Pr} (1 - \tau_{Pr} \tau_N \omega^2)}\right) \quad (31)$$

τ_N represents the time constant of the needle, i.e. $\tau_N = R_N \cdot C_N$. Similarly, $\tau_{Pr} = R_{Pr} \cdot C_{Pr}$ denotes the time constant of the voltage probe. In the next step, the voltage drop across the resistive part R_N can be calculated and hence the resistive power dissipated in the plasma P_{pl} . Mathcad[®] software¹⁹ was used to solve these equations. The resistance of the needle was calculated as 4436 Ω and its capacitance as 1 pF. The voltage drop across this resistance was 143.5 V and thus the power dissipation $P_{pl} = \frac{U^2}{R_N} = 4.6W$.

These results reveal that only a fraction, roughly one third of the power, is consumed in the needle. The remainder is dissipated elsewhere in the circuit or lost due to radiation and cable heating. Furthermore, it has to be mentioned that the inaccuracy for this kind of power calculation is relatively high due to the high capacitive nature of the device. This shall be demonstrated in the following error analysis.

5.1.1.3 Error analysis

One first source of error is the slow sampling period of the used oscilloscope that resulted in a slight signal distortion. Therefore, it was necessary to smooth the obtained results. This smoothing already affected the calculation. The peak picking was found to be

¹⁹ Mathcad, version 14.0.0.163, by Parametric Technology Corporation.

another source of error. Even though this was conducted by Origin[®] software²⁰, the results for current, voltage, and time delay deviated. The deviation of the time delay became crucial for further calculations. The sensitivity of the current probe is guaranteed by the manufacturer as $\pm 1\%$. Assuming the same for the voltage probe and a deviation of ± 0.2 ns (corresponding to 1°) for the time delay determination results in uncertainties of $\Delta U = 4.06V$, $\Delta I = 4.39 \cdot 10^{-3} A$, and $\Delta \cos(\rho) = 0.0173$. Since all variables are uncorrelated, the power uncertainty ΔP is calculated as follows:

$$\Delta P = \pm \sqrt{\left(\left(\frac{\partial P}{\partial U}\right) \cdot \Delta U\right)^2 + \left(\left(\frac{\partial P}{\partial I}\right) \cdot \Delta I\right)^2 + \left(\left(\frac{\partial P}{\partial \rho}\right) \cdot \Delta \cos(\rho)\right)^2} \quad (32)$$

with

- $\frac{\partial P}{\partial U}$, $\frac{\partial P}{\partial I}$, and $\frac{\partial P}{\partial \rho}$ denoting the partial derivatives of $P = U \cdot I \cdot \cos(\rho)$ and
- ΔU , ΔI , and $\Delta \cos(\rho)$ the uncertainties.

Solving this equation with the uncertainties given above and the measured means results in

$$\Delta P = \pm \sqrt{(0.1584W)^2 + (0.1584W)^2 + (-3.0843W)^2} \approx 3.1W \quad (33)$$

This is almost 20% of the earlier calculated power P of 15.8 W. If the uncertainty of the time delay is set to 0.5 ns, the power uncertainty increases to $\Delta P = 7.5W$ which is already 48% of the earlier calculated power value. Hence, it is obvious that the power uncertainty mainly originated from the uncertainty of the phase angle. A slight change of the phase angle is amplified by the cosine function. Thus, the use of an oscilloscope with a higher sampling period and an embedded peak picking function is desirable and recommended for further experiments in order to reduce this error source.

5.1.2 Temperature measurements

Since the RF-emission of the plasma-needle was influencing this measurement while using a thermocouple, the temperature of the gas stream was measured with a simple mercury thermometer. The heat-sensitive part of the thermometer was placed in the gas stream at different distances. The power delivered to the plasma was increased meanwhile the temperature was recorded. Experiments were conducted for a pure helium plasma and

²⁰ OriginPro 7.5SR0, by OriginLab Corporation.

for the two helium-cyclohexane mixtures. Due to the imprecise nature of this measurement method, results can only be discussed as approximations to the accuracy of a thermocouple.

5.1.2.1 Pure helium plasma

The distance describes the gap between the needle-tip and the surface of the thermometer. With higher power the size of the plasma plume increased and extended to the thermometer's surface. Arranging the thermometer closer to the plasma plume results in an increase of temperature. The temperature differences between the 7 mm and the 10 mm measurement were marginal and within the resolution of the thermometer. An almost linear dependence between power and temperature was observed. The results for 5 mm and 3 mm, respectively, on the other hand showed a non-linear correlation between power and temperature. Especially in case of a 3 mm gap, the temperature increased rapidly from 82 °C at 12 W to 134 °C at 15 W. Figure 31 shows the gas stream temperatures of a pure helium plasma. The temperature as a function of power for a pure helium plasma is presented in figure 32.

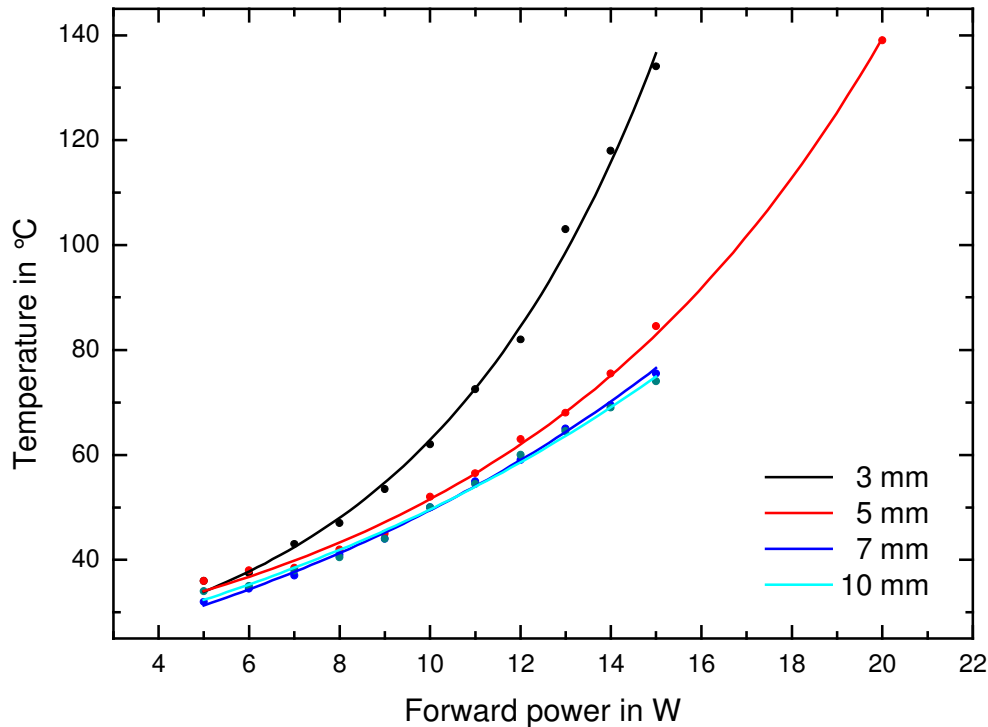


Fig. 31: Temperature as function of distance between the needle-tip and the surface of the thermometer for a pure helium plasma

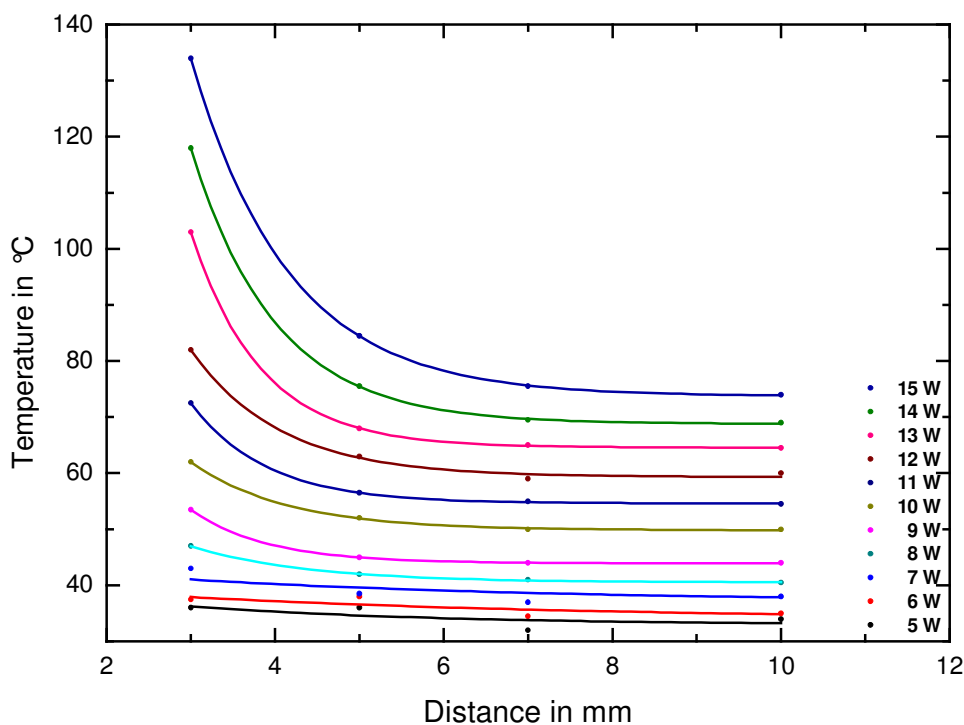


Fig. 32: Temperature as function of power for a pure helium plasma

5.1.2.2 Helium – cyclohexane mixture plasma

Figure 33 illustrates the gas stream temperatures of helium plasmas with different admixtures of cyclohexane. The distance between the needle-tip and the surface of the thermometer was fixed at 5 mm. The results for admixtures of 7 sccm and 35 sccm cyclohexane showed a similar characteristic. The temperature increased almost in parallel with a higher slope above 15 W delivered power. The obtained temperature for the admixture of 35 sccm cyclohexane on average is 10°C higher than for 7 sccm. This could be due to the high heat conductivity of helium. The relative content of helium for an admixture of 35 sccm cyclohexane is lower than for 7 sccm resulting in a reduced heat conductivity of the gas mixture and a higher temperature measured. Furthermore, the temperatures of the mixtures are remarkably lower than the temperature of the pure helium discharge. This can be ascribed to the energy which has to be brought up for the dissociation of the cyclohexane molecule.

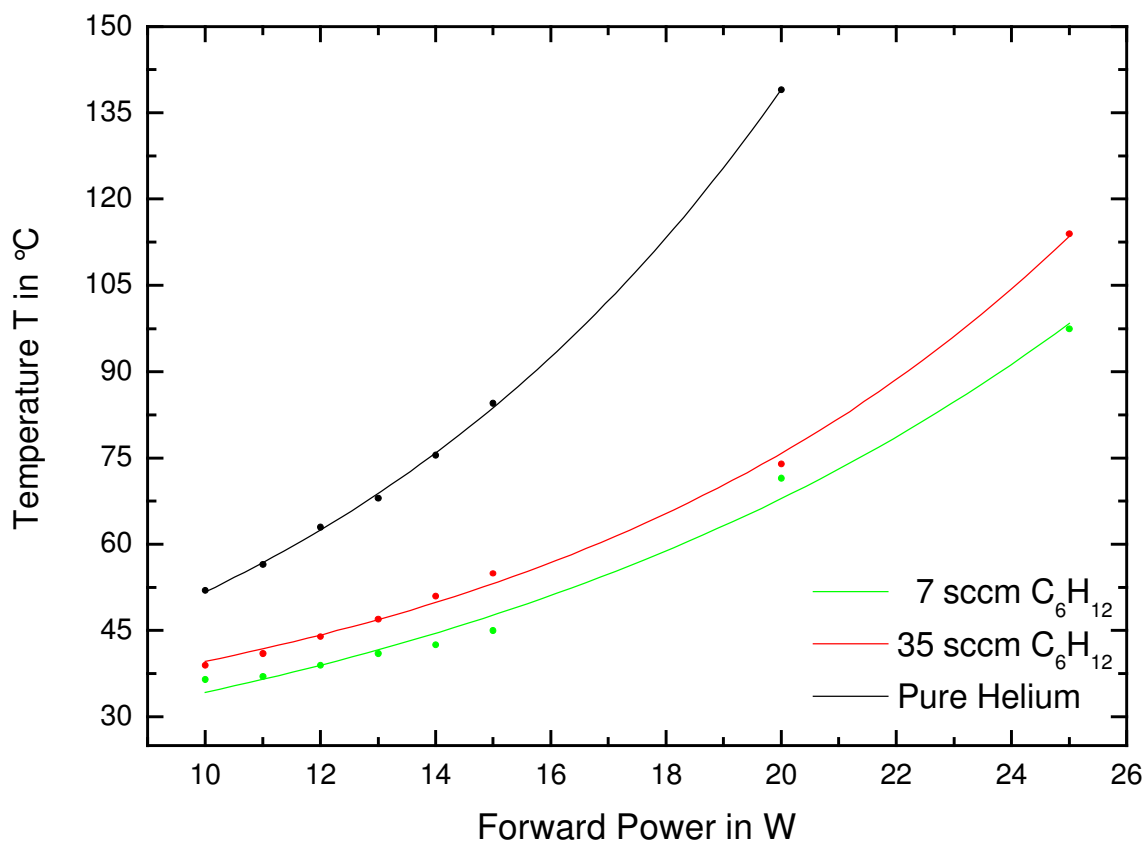


Fig. 33: Temperature of helium discharges with admixture of cyclohexane

5.1.3 Optical emission spectroscopy

Spectra of a pure helium plasma and a helium-cyclohexane plasma were recorded in the range from 200 nm to 800 nm using an USB2000 Miniature Fiber Optic Spectrometer from Ocean Optics. The USB2000 is a low resolution spectrometer with a resolution of 1.5 nm. It operates with a 2048-element linear CCD-array as light detector. The light emission was collected using an optical fiber with a collimating lens, which was arranged on axis and aligned 40 mm from the end of the plasma-needle. The integration time was 165 ms. The emission spectrum of the pure helium plasma is presented in figure 34. Intense emission lines could be ascribed to O^* , He , N_2^+ , N_2 and OH^- [26]. Emissions of OH^- are generally found when water vapour is present, which is ubiquitous in an open-air system. The presence of the N_2 and N_2^+ is due to the surrounding air as well. The intensity of the nitrogen lines was dominant over the helium lines indicating that the discharge was not only based on helium [27]. Thus, the existence of polar groups such as OH^- could be verified, which are responsible for the effects utilized for surface modification (5.2.1). Fur-

thermore, long wave UV-emission could be detected in the range between 400 nm and 300 nm.

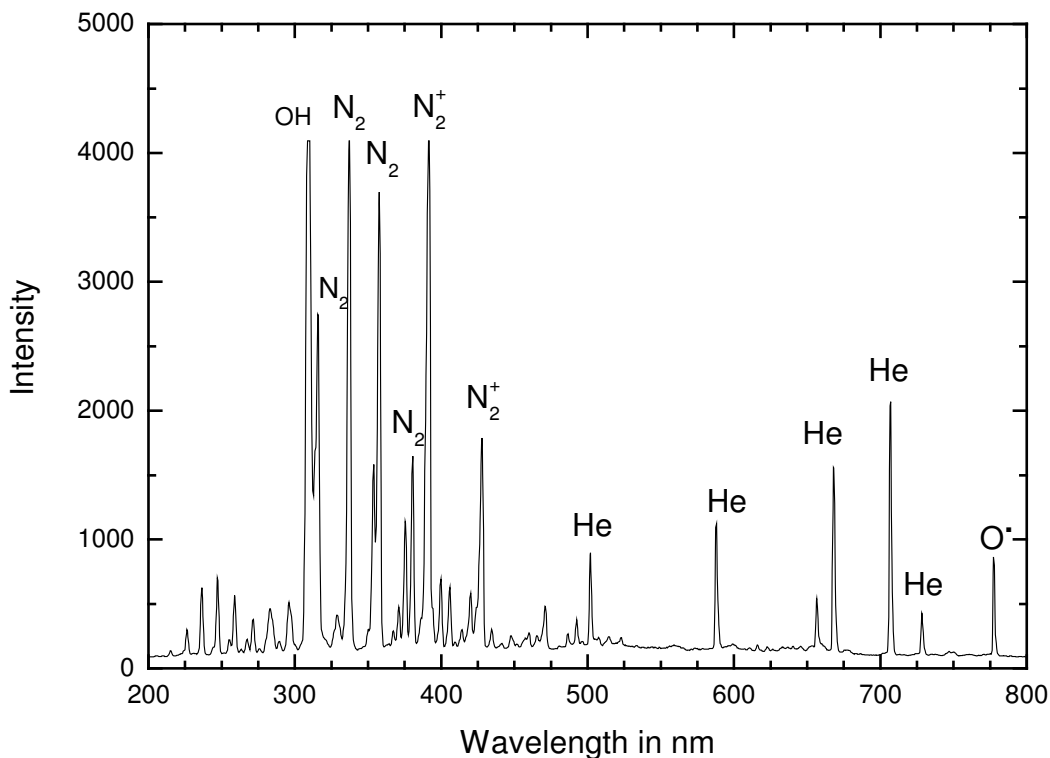


Fig. 34: Emission spectrum of the plasma-needle for a pure helium plasma

The emission spectrum of a helium-cyclohexane plasma with admixture of 7 sccm C₆H₁₂ was recorded and is shown in figure 35. This experiment was executed in a chamber in order to obtain more information about the oxygen contamination of the deposited carbon films²¹. The chamber was flooded with helium, a little aperture in the bottom prevented overpressure. In contrast to the pure helium plasma, the intensity of the helium peaks dropped. This peak disparity in the visible range from 400 nm to 700 nm comes along with a change in colour of the plasma as described in chapter 4.1. Furthermore, the OH⁻-line at 308.6 nm and the O⁺-line at 777.5 nm were reduced significantly that can be explained with the absence of air. Surprisingly, no lines of carbon-containing groups as for example CH (at 431 nm, 389 nm, 387 nm, 315 nm), CO (system of single-headed bands extending from 280 nm to 100 nm), or CH₂ (many-line structure between 537 nm and 819 nm) [cp.

²¹ As the FTIR-results in chapter 5.2.2.2 revealed, the carbon films contained a lot of oxygen. Delayed FTIR-scans and the above presented OES-experiment were conducted in order to discover the source of this contamination.

26] could be observed. This might be either due to blending by the nitrogen peaks or the low resolution of the spectrometer and a comparable low intensity of those groups.

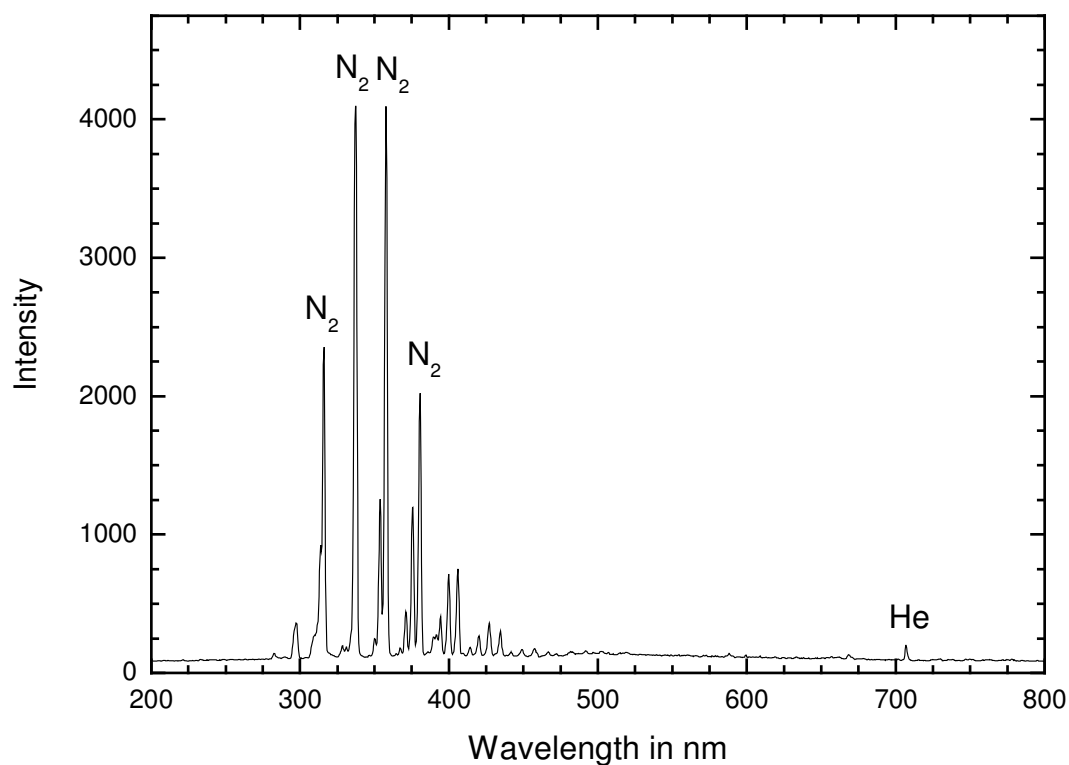


Fig. 35: Emission spectrum of a helium-cyclohexane plasma

PART III

5.2 Plasma-needle applications

5.2.1 Surface modification

5.2.1.1 Contact angle measurements of various substrates after helium plasma treatment

Samples of different materials were treated with the plasma-needle to test its possible application for surface modifications. The substrates were cleaned in an ultrasonic bath with soap-containing solution. Afterwards, they were dried with ethanol and nitrogen. The plasma treatment lasted for a couple of seconds at 15 W. No reactive gas has been added. Pictures of the samples before and after treatment are shown below (figures 36 to figure 41). They were also used to determine the contact angle.

The substrates showed different contact angles before treatment: the Millipore petri dish had a hydrophobic character with a contact angle of 71° . On the other hand, silicon with a contact angle of 21° could already be classified as hydrophilic. All other substrates ranged between 32° and 45° . Since all substrates were cleaned before plasma treatment, the different contact angles can be ascribed only to the roughness and the chemical composition of the substrates. Due to the drying with ethanol, no impurities containing polar groups were expected on the surfaces. Substrates with a very smooth surface, like silicon or quartz showed a minor contact angle than samples with a comparable rough surface, like the copper samples. The hydrophobic character of the Millipore petri dish is mostly due to the chemical characteristic of the material. The petri dish is made of polystyrene, a polymeric hydrocarbon that does not contain any polar groups.

In every case a reduction of the contact angle below 30° was observed after plasma treatment. Major improvements were observed for the Millipore petri dish (from 71° to 20°) and the quartz (from 32° to 7°). The effect on the silicon (from 21° to 18°) was within the accuracy of the measurement. These results are summarized in table 5.

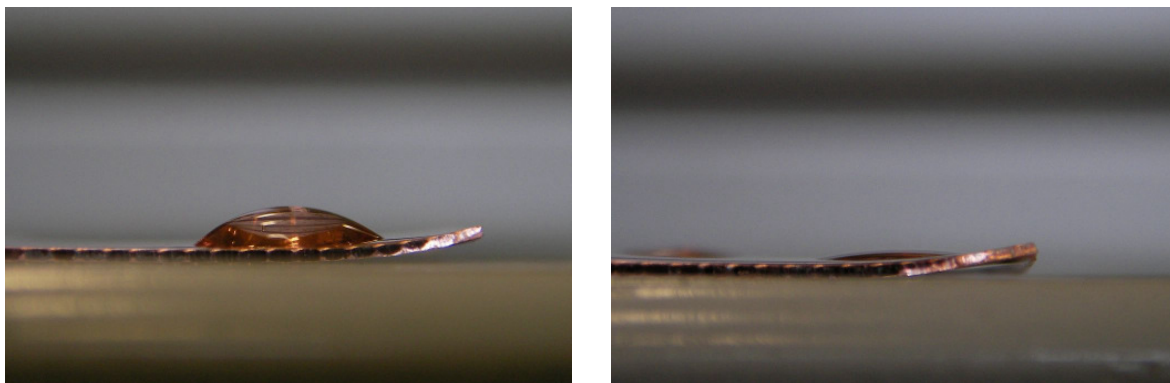


Fig. 36: Thin copper untreated (left) and treated (right)

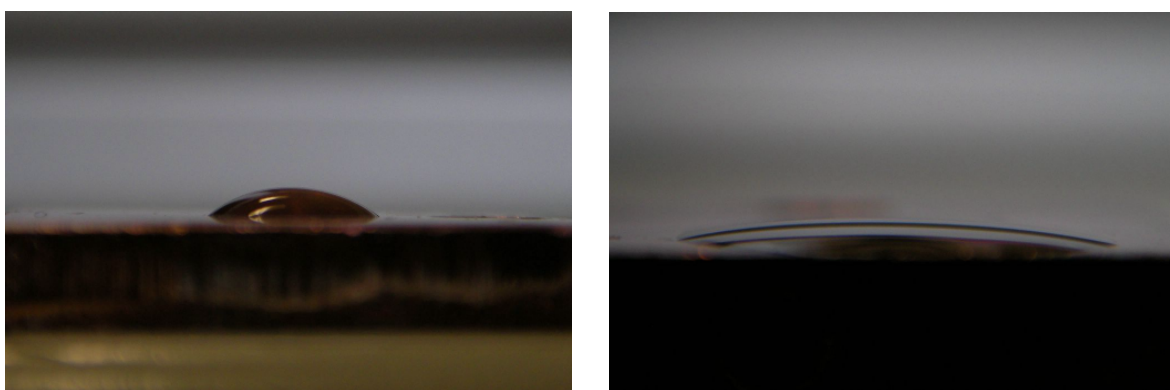


Fig. 37: Thick copper untreated (left) and treated (right)

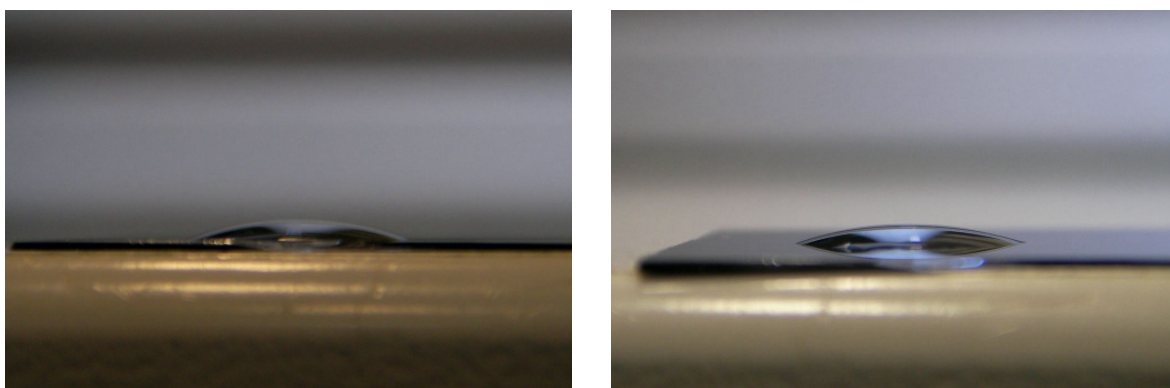


Fig. 38: Silicon untreated (left) and treated (right)

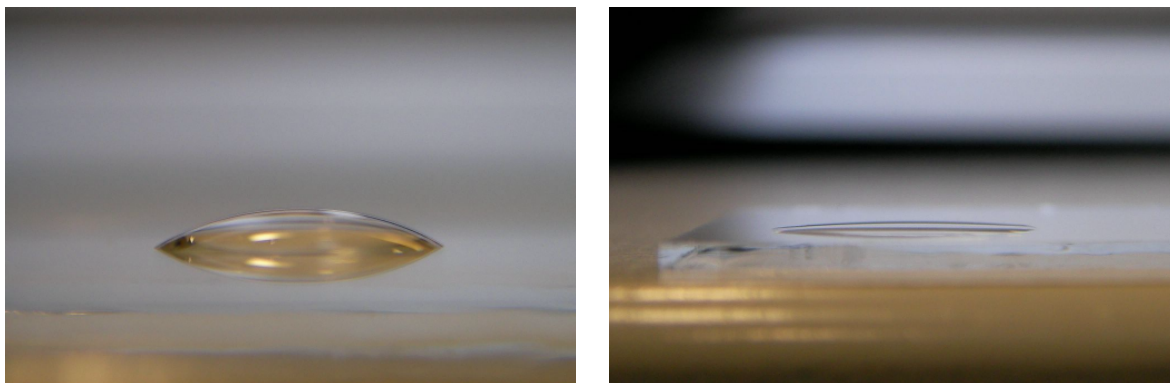


Fig. 39: Quartz untreated (left) and treated (right)

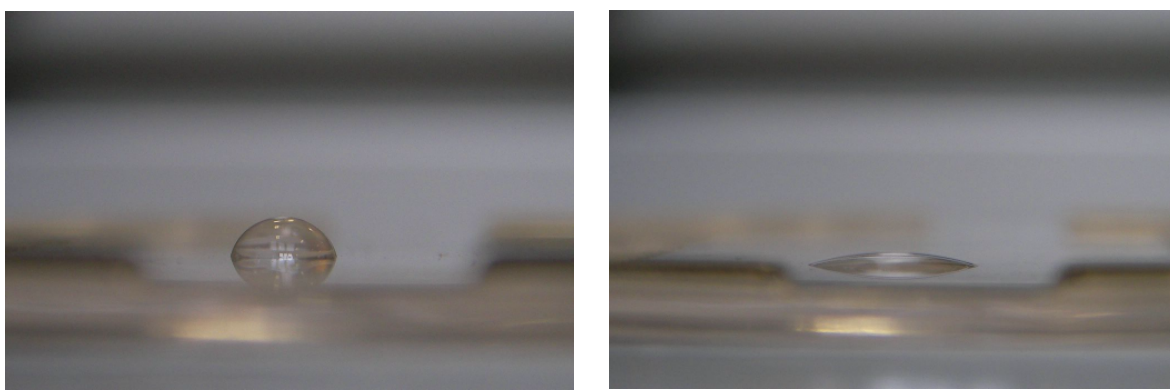


Fig. 40: Millipore petri dish untreated (left) and treated (right)

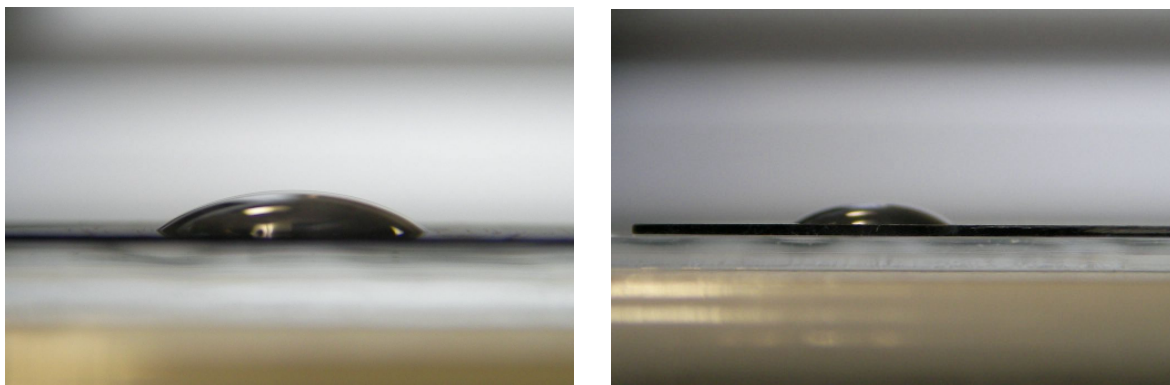


Fig. 41: Polymer-like hydrogenous amorphous carbon deposited on silicon untreated (left) and treated (right)

Tab. 5: Results of contact angle measurements

Material	Angle untreated [°]	Angle treated [°]
Thin copper	45	13
Thick copper	43	not measurable
Silicon	21	18
Quartz	32	7
Millipore petri dish	71	20
Polymer-like a-C:H on silicon	40	29

Since the plasma treatment is not significantly affecting the roughness of the samples, the improved hydrophilicity can only be ascribed to the increased presence of polar groups, like OH^- and O^* after the treatment on the surface. The results of the optical emission spectroscopy verified the presence of these species in the plasma. It has to be pointed out that the contact angle of silicon coated with a polymer-like hydrogenous amorphous carbon film before the treatment was twice as much as in case of pure silicon. Thus, the coating with a carbon film made the substrate surface more hydrophobic.

5.2.1.2 ELISA results

Treatment time and power settings were chosen as presented in table 6.

Tab. 6: Settings for ELISA experiment

Run	Treatment time in seconds	Plasma power in W	Time between plasma treatment and ELISA
I	0 (Control)	---	---
II	60	10	140 min
III	120	10	120 min
IV	60	15	100 min
V	120	15	80 min
VI ²²	10	20	60 min

²² This treatment was done with a diffused plasma generated by an external helium flow *around* the needle.

The results of the ELISA are presented in figure 42. In contrast to the untreated control, the plasma treated microtiter plates showed a significantly lower value of absorbance. Augmented hydrophilicity of the surface due to the presence of polar groups (for example OH , O^{\bullet}) and therefore less affinity to molecules that contain both hydrophilic and hydrophobic groups as IgG are a reasonable explanation for this observation. Hence, the enormous decrease of absorption is caused by a lack of adsorbed molecules to the microtiter plate. The decrease of affinity correlates directly with the plasma power and is inversely proportional to time that passed between plasma treatment and absorption measurement. It is remarkable that in case of the diffuse plasma treatment, the effect is even more evident than in all other cases although the exposure time was only a fraction.

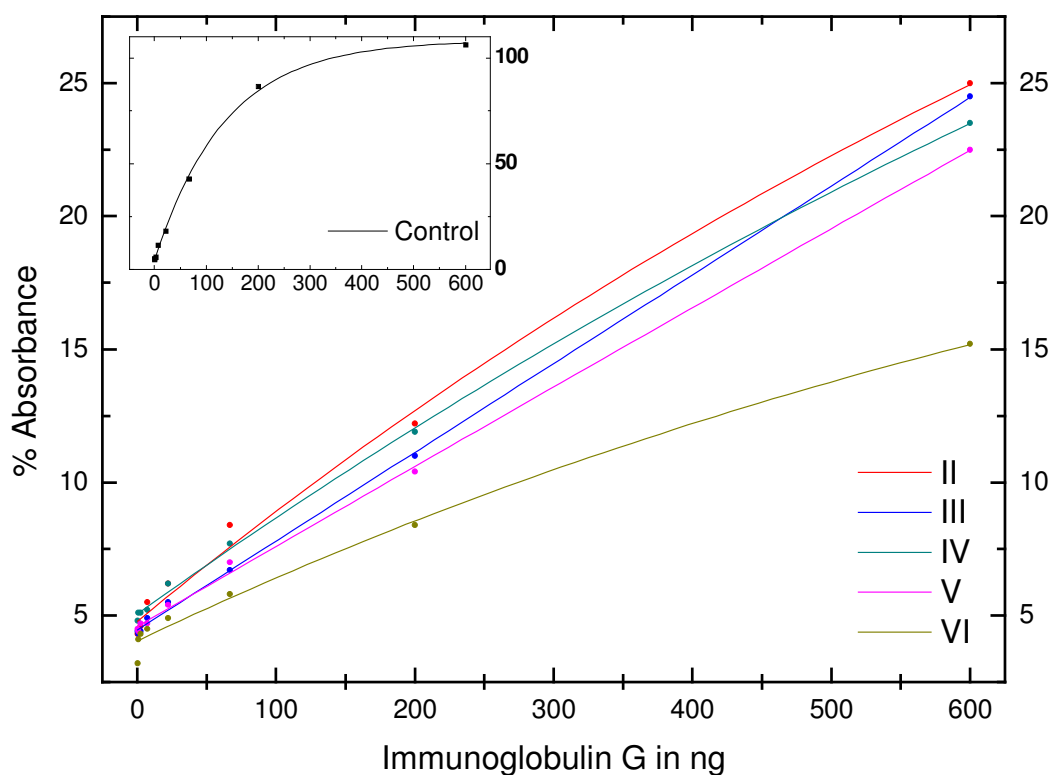


Fig. 42: ELISA results

This experiment emphasises that for protein binding a surface must be moderately hydrophilic. A strong hydrophilic surface works in the same way as a hydrophobic. Even though these results are the direct opposite of the desired effect, they demonstrate impressively the influence of a plasma treatment on surfaces and suggest a potential future application when protein binding on culture substrates is needed to be inhibited.

5.2.2 Carbon film deposition

In order to examine potential applications of the plasma-needle as a deposition tool, it was attempted to deposit DLC-layers on quartz substrates. As mentioned earlier, cyclohexane was chosen as carbon-containing precursor gas, since it is easy to handle and little research has been conducted on using cyclohexane as carbon source in a plasma-needle. Different amounts of cyclohexane were added to the helium flow.

The two pictures below show such a deposition (see figure 43). It has to be noted, that the covered area on these pictures did not result from a static treatment. The substrate was mounted on the axis of a rotating step motor and the plasma-needle was positioned approximately two millimetres eccentric. This arrangement enabled the coating of a greater area, which was required for the FTIR-analysis, without manipulating the device.

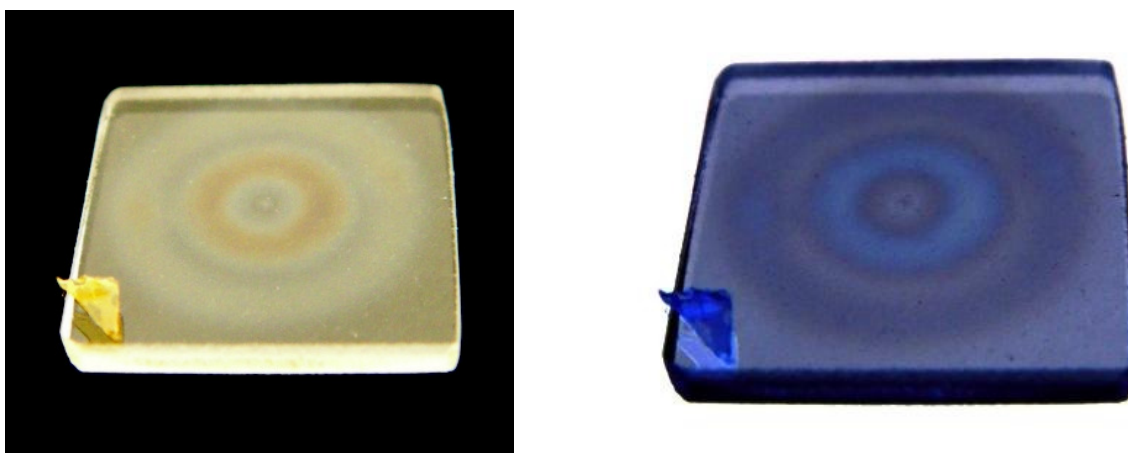


Fig. 43: Example of a deposited film (left), same example with inverted colours (right)

5.2.2.1 Profiles and deposition rates

In order to estimate the deposition rate of the plasma-needle, samples were exposed to the cyclohexane-helium-plasma at 20 W. The plasma-needle was positioned perpendicular to the substrate. The distance between the capillary tip and the surface of the samples was kept constant at 2.5 mm. At this distance and power the plasma plume was barely encountering the surface. The exposure time was varied between one and five minutes in steps of one minute. The bypass-valve was completely opened giving rise to a cyclohexane flow of 35 sccm.

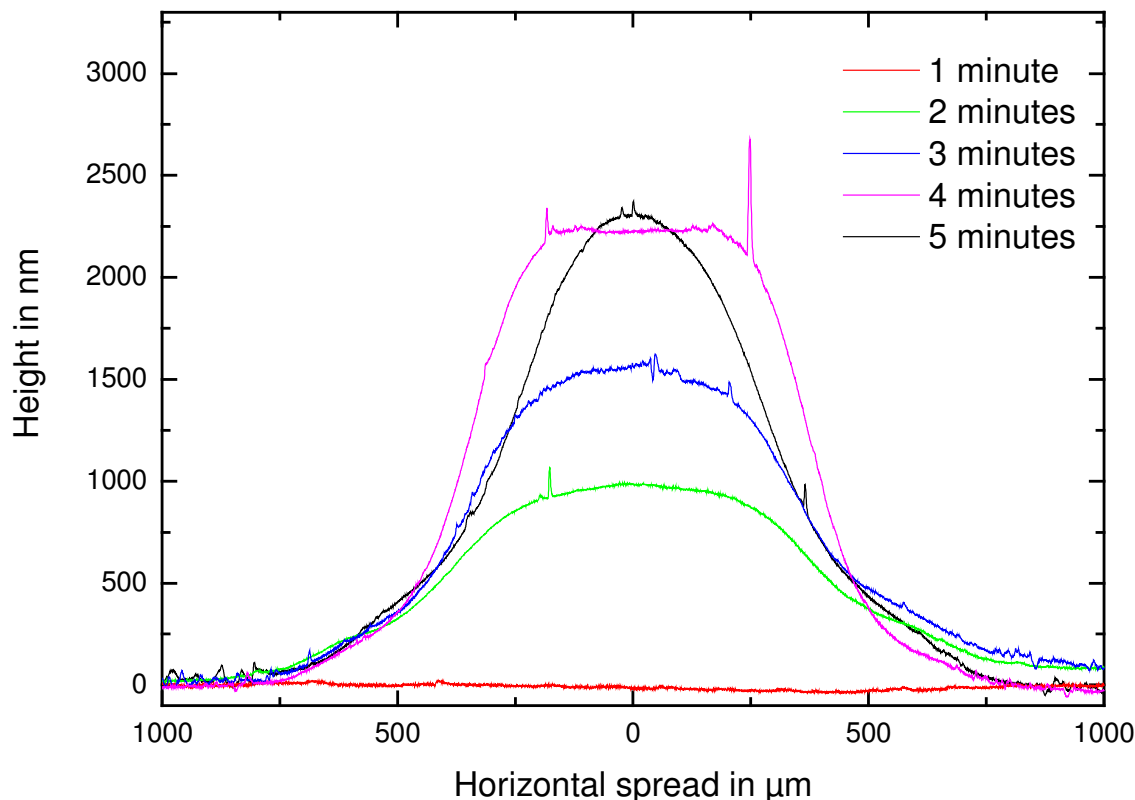


Fig. 44: Profiles of different films deposited at 20 W and 35 sccm cyclohexane

The obtained profiles as presented in figure 44 show a peaked distribution except the one after four minutes treatment, which has not developed a real peak but a plateau. The horizontal spread was around 1 mm which corresponds to the diameter of the capillary. No measurable film was obtained after a treatment of one minute. This can be explained with a lack of crystal grains on the clean substrate which would act as growth catalysts. Furthermore, the attachment of the carbon species is probably based on weak van-der-Waals forces and not due to chemical bonds. Thus, it is difficult for the carbon species to attach to the blank substrate surface. But as soon as the first atoms have attached to the substrate, the growth of further layers is facilitated. With increasing treatment time the peak of the films heightened from ≈ 1000 nm for 2 minutes to ≈ 1600 nm for 3 minutes, the plateau height at ≈ 2200 nm after 4 minutes finally to ≈ 2350 nm for 5 minutes. These results allow the estimation of a deposition rate of roughly 550 nm/min.

The results for a cyclohexane flow of 7 sccm revealed a similar characteristic except for one film whose profile had a shallow minimum on its symmetric axis. An almost linear correlation between treatment time and peak height was observed. Peaks were estimated as ≈ 1500 nm for 90 seconds treatment, ≈ 1950 nm for 120 seconds, ≈ 2600 nm for

150 seconds, and ≈ 3200 nm for 180 seconds giving rise to an estimated deposition rate of ≈ 1000 nm/min.

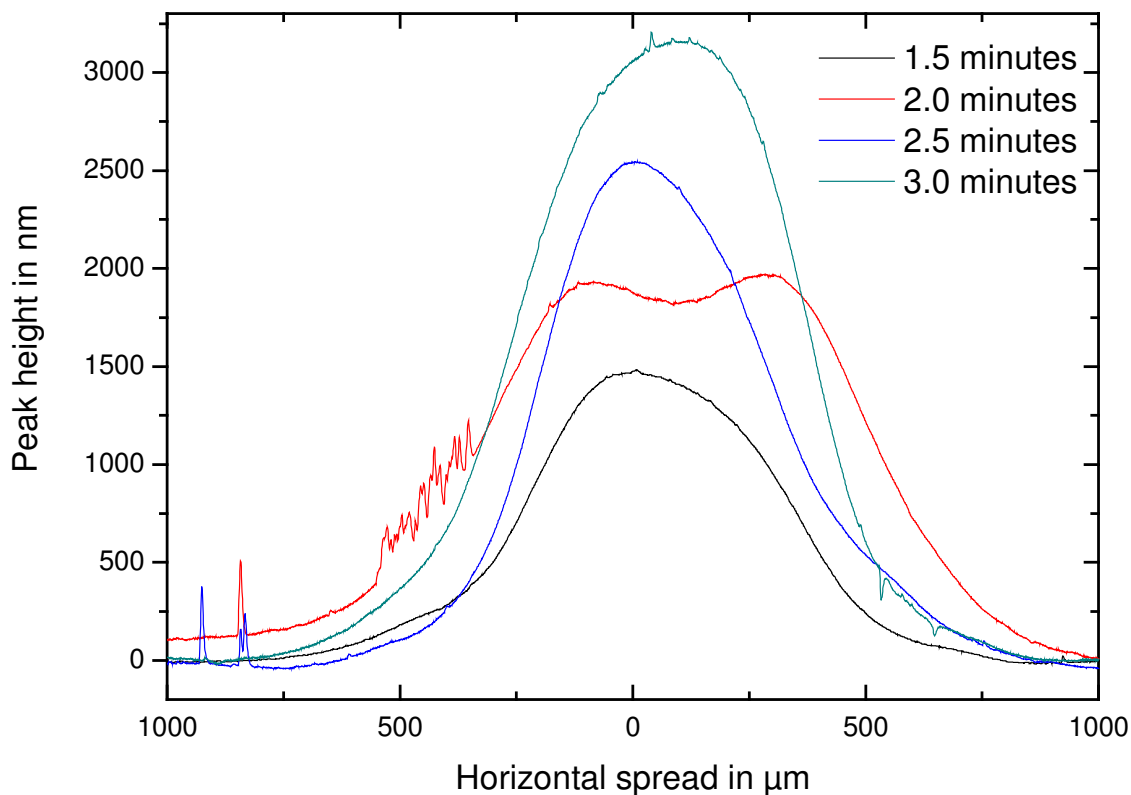


Fig. 45: Profiles of different films deposited at 20 W and 7 sccm cyclohexane

Thus, the deposition rate seems to be higher for a lower content of cyclohexane. Responsible for film deposition is not the content of reactive gas, but the content of dissociated species in the gas stream. If the plasma's energy content is not sufficient to dissociate all cyclohexane molecules, these molecules do not contribute to the film deposition. This assumption is underlined by the experimental observation of a decreasing plume size illustrated in figure 13.

Even though a higher deposition rate was achieved with a reduced content of cyclohexane in the gas mixture, adding more cyclohexane to the gas mixture seems more recommendable since the deposited profiles are more uniform and a deposition rate of approx. 550 nm/min is satisfying.

5.2.2.2 FTIR

FTIR-spectra were recorded in the $4000\text{-}1000\text{ cm}^{-1}$ range using a Jasco FTIR 660 Plus spectrometer with a resolution of 4 cm^{-1} . The sample cell and the interferometer were evacuated in order to prevent absorption peaks of water and atmospheric gases. Films were deposited on silicon at 15 W, with 35 sccm cyclohexane and a deposition time of six minutes. Figure 46 depicts the baseline-corrected spectra of a deposited film. The broad intense band at around 3350 cm^{-1} (-O-H stretching) can be ascribed to the presence of primary or secondary alcoholic groups. Sharp and strong peaks could be found at 2938 cm^{-1} (asymmetric -C-H stretching) and 2860 cm^{-1} (symmetric -C-H stretching) which can be assigned to the carbon-hydrogen stretching of a methyl group. The strong peak at 1722 cm^{-1} was unambiguously identified as a ketone-like carbonyl group. Another less expressed peak was found at 1452 cm^{-1} (bending of -C-H). These spectral features indicate the presence of an aliphatic, soft, polymer-like structure, without C=C double bonds (absence of H-C=C stretching above 3000 cm^{-1} and absence of C=C stretching between 1670 cm^{-1} to 1640 cm^{-1}) [cp. 28].

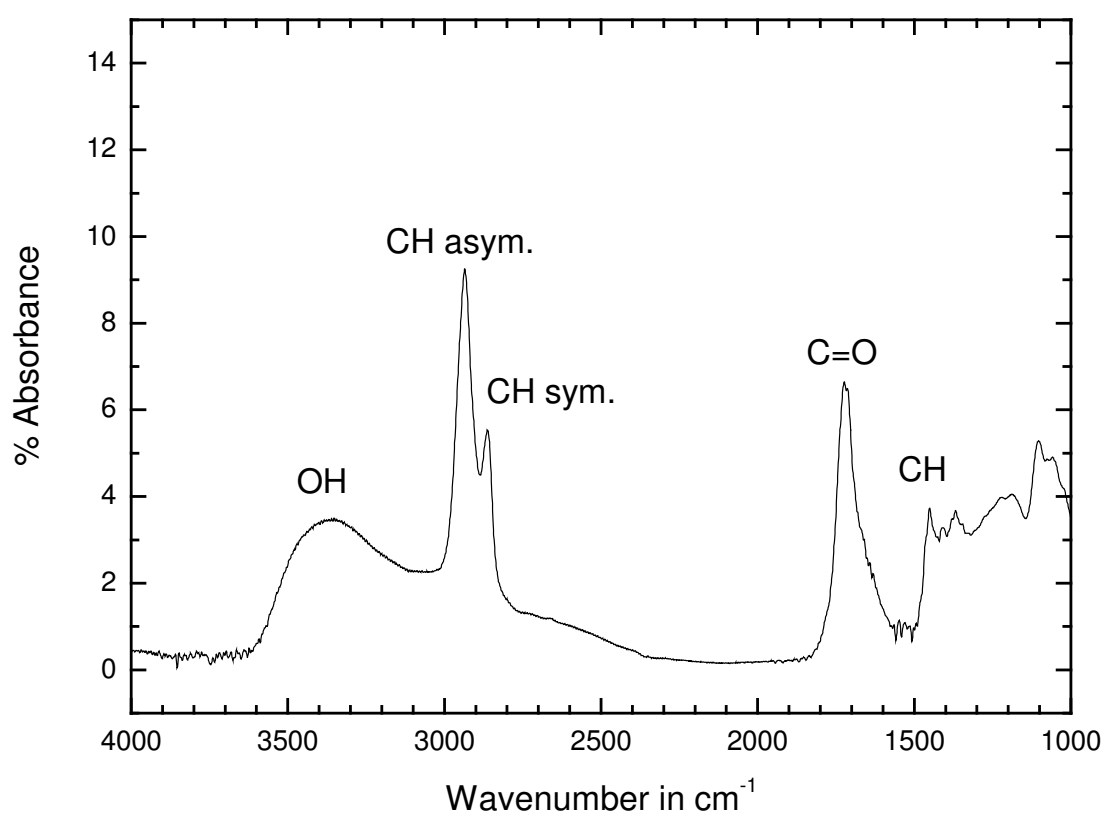


Fig. 46: FTIR-spectrum of an a-C:H film deposited in air

However, a considerable high presence of bonded oxygen was observed. This was also observed by BENEDIKT ET AL. [29], who conducted further depositions in a pure argon atmosphere in order to exclude the oxygen presence in their film due to a contamination from the surrounding air. Their FTIR-results still revealed the presence of oxygen which then was ascribed to an oxidation of the carbon film after deposition.

To validate this assumption, another deposition in a protective helium-atmosphere was conducted and further FTIR-scans were performed: the first immediately after the deposition, others 5 minutes, 60 minutes, and one week afterwards. Figure 47 presents baseline-corrected FTIR-scans of a film deposited in air and one in a helium-atmosphere. The latter was performed immediately after deposition.

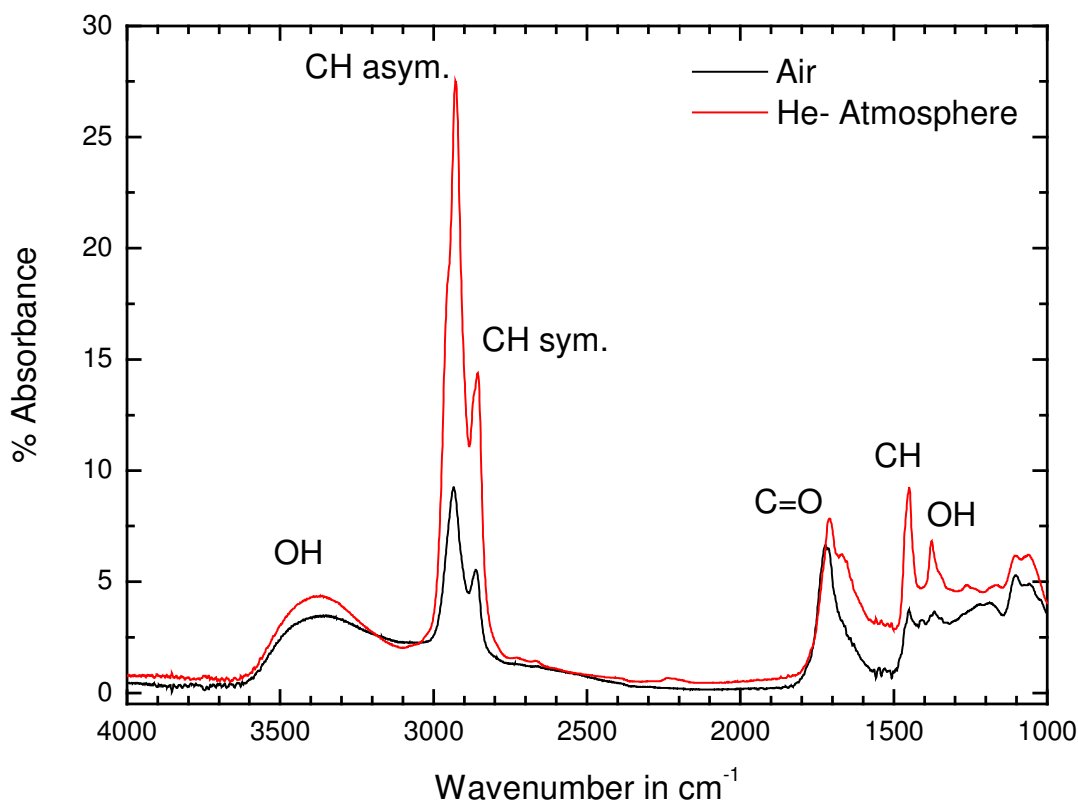


Fig. 47: FTIR-spectra of two a-C:H films deposited in different atmospheres

Even though both films display the same infrared features, the CH-peaks are substantially more evident in case of a protective helium-atmosphere deposition, or in other words, the content of bonded oxygen was reduced. To compare the results, the area of the broad OH-peaks and of the CH-peaks (at 2938 cm^{-1} and 2860 cm^{-1}) as well as the peak heights of the C=O- and the CH-peak at 1452 cm^{-1} were measured. The obtained results for the deposition in air were used as a reference.

As presented in figure 48, the presence of oxygen was reduced and did not change significantly over time.

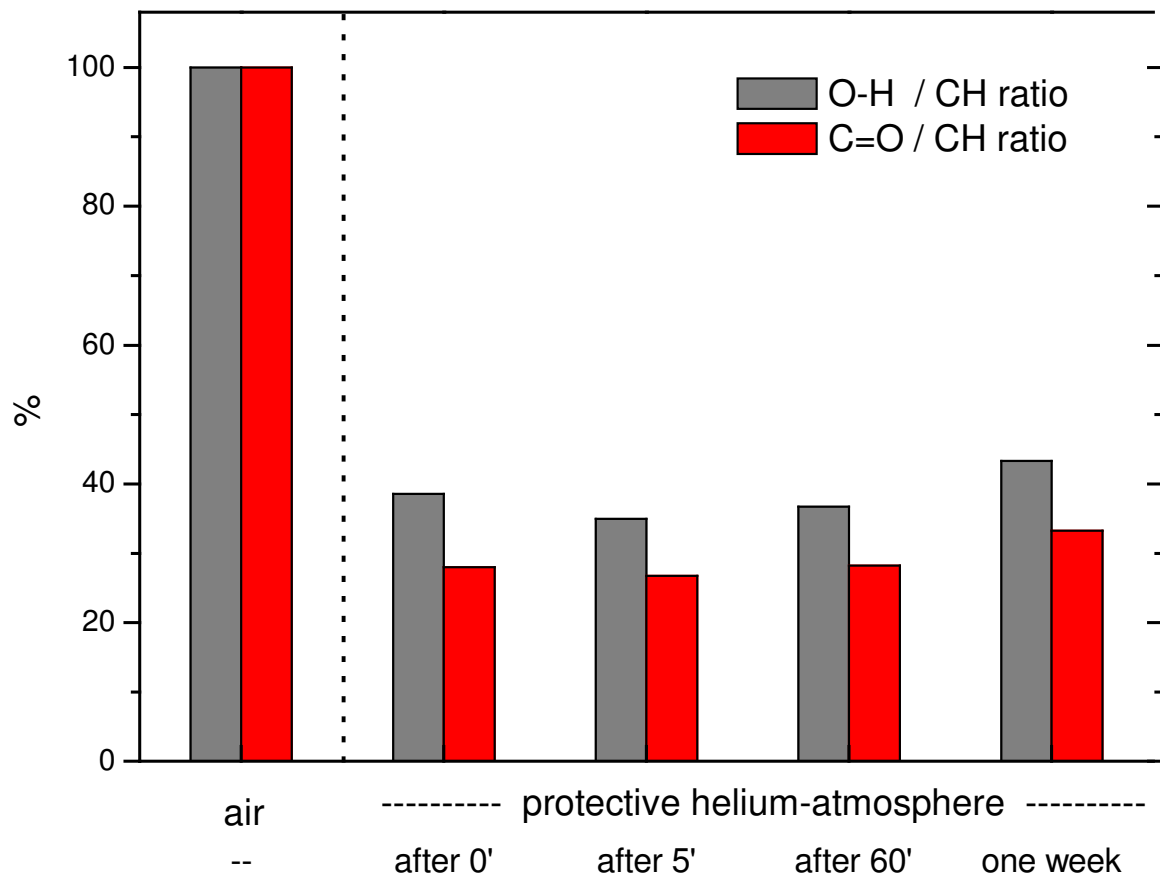


Fig. 48: Reduction of oxygen-containing groups

These results are oppositional to the ones described by BENEDIKT ET AL. [29]. In this case it seems that the oxygen bonding only occurs during the plasma process and not afterwards. The remaining presence of oxygen-containing groups could be due to residual-oxygen in the gas lines or in the deposition chamber, which has not been evacuated but only flooded with helium. However, a proceeding oxidation of the film also depends on the film's properties like its porosity for example. Thus, both assumptions may be correct and should be validated in future experiments.

6 Conclusions

A new plasma-needle has been developed within the scope of this work that can be operated at atmospheric pressure. The manifold biomedical applications of such plasma sources were presented and experimentally proven for thin film deposition and surface modification.

Due to the uncertain determination of the phase shift, the results of the electrical measurements are only partly meaningful. The capacitive character of the plasmas source could be confirmed with the help of these electrical measurements and the breakdown voltage could be identified as $U = 274V_{pk-to-0}$. An exemplary calculation of the power dissipation revealed, that only a fraction of the total power is dissipated in the plasma itself. However, this kind of power calculation is very inaccurate due to sensitivity of the cosine for capacitive devices.

As expected, the temperature of the gas stream increased with higher forward power. A linear dependence between temperature and power was observed at a distance of 10 mm. This dependence changed to an exponential character for lower distances. The temperature rose from 40 °C up to 140 °C. The admixture of cyclohexane resulted in a temperature lowering of approximately 10 °C. This can be explained with the energy that is required for the dissociation of the cyclohexane.

The results of the optical emission spectroscopy were typical for a plasma-needle operating in open air. Peaks could be ascribed to atomic helium, oxygen, and nitrogen as well as to OH^- - and N^+ -ions. The comparable intense nitrogen peaks allow the assumption that the discharge is not only sustained by helium. Furthermore, the presence of OH^- -ions explained the surface modification by the plasma-needle.

The plasma-needle was tested for surface activation and for carbon film deposition. It was possible to use the plasma-needle with cyclohexane as reactive gas to deposit amorphous carbon layers. Measurements of the deposition rate revealed a dependence of the cyclohexane content in the gas mixture, whereas a lower content of reactive gas gave rise to a greater deposition rate. An analysis of such deposited films using FTIR-spectroscopy revealed that all these films were polymer-like. Generally, films with a higher hardness are of higher interest for practical purposes. The oxygen contamination of the films could be reduced by deposition in a protective helium atmosphere.

A proceeding oxidation of the films after the deposition was analyzed by delayed FTIR-scans and could be excluded. This allows the conclusion that the oxygen contamination mainly occurred during the deposition.

Potential applications of the plasma-needle in terms of surface modification were studied executing contact angle measurements on various materials. The plasma treatment gave rise to a reduction in contact angle, or in other words, to a higher surface energy for all materials. This effect is due to the presence of OH^- -ions. Additionally, a microtiter plate, which is often used in biochemistry and related scientific fields, was treated. The observed increased hydrophilicity of the wells caused a diminished adhesion of immunoglobulin G.

It is desirable for prospective applications to deposit films with higher quality and purity as well as to cover greater areas. The latter can be achieved by constructing an array of several plasma-needles or by redesigning the present plasma-needle source. In order to conduct more precise electrical measurements an oscilloscope with a significantly higher sample rate is essential. Furthermore, it is advisable to use an RF-generator and an adequate matching network which have been constructed especially for low power applications such as a plasma-needle. However, the present development stage of the plasma-needle allows its utilization for experiments on the interaction between plasma and cells/biological tissue.

6.1 Zusammenfassung

Im Rahmen dieser Arbeit wurde eine Plasma-Nadel entwickelt, die bei Atmosphärendruck operieren kann. Die vielfältigen biomedizinischen Anwendungsmöglichkeiten derartiger Plasmaquellen wurden dargestellt und anhand von Experimenten auf dem Gebiet der Schichtabscheidung und Oberflächenmodifikation bestätigt.

Mittels elektrischer Messungen konnte der kapazitive Charakter der Plasmaquelle und die Durchbruchsspannung zu $U = 274V_{pk-to-0}$ belegt werden. Eine beispielhafte Berechnung der Leistungsaufnahme zeigte, dass nur ein Bruchteil der Gesamtleistung im Plasma selbst verbraucht wird. Einschränkend ist anzumerken, dass diese Art der Leistungsermittlung wegen der Empfindlichkeit der Kosinusfunktion für kapazitive Konstruktionen äußerst fehlerbehaftet ist.

Erwartungsgemäß erhöhte sich die Temperatur des Gasflusses mit zunehmender eingekoppelter Leistung. Bei einem Thermometerabstand von 10 mm erwies sich dieser Zusammenhang als linear. Für geringere Abstände zeigte sich ein exponentieller Temperaturanstieg. Dabei stieg die Temperatur von rund 40 °C auf bis zu 140 °C. Die Zuführung von Cyclohexan resultierte in einer Verringerung der Temperatur um etwa 10 °C. Energetisch betrachtet kann dies mit dem Energieaufwand erklärt werden, der zur Dissoziation des Cyclohexans benötigt wird.

Die Messungen mittels der optischen Emissionsspektroskopie lieferten für eine derartige Plasmaquelle typische Spektren. Die Peaks konnten atomarem Helium, Sauerstoff und Stickstoff sowie OH^- - und N^+ -Ionen zugeschrieben werden. Die vergleichsweise intensiven Stickstoffpeaks lassen vermuten, dass die Entladung nicht ausschließlich vom Helium erhalten wird. Weiterhin konnte mit der Präsenz der OH^- -Ionen die oberflächenmodifizierende Wirkung des Plasmas erklärt werden.

Die Plasma-Nadel konnte mit Cyclohexan als reaktivem Gas zur Schichtabscheidung von amorphen Kohlenstoffschichten verwendet werden. Es zeigte sich, dass die Schichtabscheidungsrate abhängig vom Cyclohexananteil im Gasmisch ist, wobei eine höhere Rate für einen geringen Anteil an reaktivem Gas ermittelt wurde. Eine Analyse der abgeschiedenen Filme mittels FTIR-Spektroskopie ergab, dass die abgeschiedenen Schichten alle polymerartig sind. Generell sind härtere Schichten aber für praktische Anwendungen von größerem Interesse. Das Vorhandensein von Sauerstoff in den abgeschiedenen

Kohlenstoffschichten konnte durch eine Deposition in einer Heliumatmosphäre reduziert werden. Eine fortschreitende Oxidation der Filme nach der Abscheidung wurde mit zeitversetzten FTIR-Analysen untersucht und konnte nicht bestätigt werden. Dies erlaubt den Rückschluss, dass die Sauerstoffkontamination der Schichten lediglich während der Abscheidung geschieht.

Anwendungsmöglichkeiten der Plasma-Nadel zur Oberflächenmodifikation wurden anhand von Kontaktwinkelmessungen bei unterschiedlichen Materialien untersucht. Die Plasmabehandlung führte bei allen Materialien zu einer Abnahme des Kontaktwinkels bzw. zu einer Zunahme der Oberflächenenergie. Dies ist der Präsenz der OH^- -Ionen zuzuschreiben. Zudem wurden einzelne Wells einer Mikrotiterplatte, wie sie häufig in der Biochemie und verwandten Wissenschaften verwendet wird, behandelt. Die dadurch resultierende Hydrophilisierung der Wells führte in diesem Fall zu einer erheblich verminderten Adhäsion von Immunoglobulin G.

Für zukünftige Anwendungen ist es wünschenswert, sowohl eine höhere Qualität und Reinheit der Schichten zu gewährleisten als auch eine größere Oberfläche beschichten zu können. Letzteres kann beispielsweise durch Zusammenschalten von mehreren Plasma-Nadeln oder durch Neugestaltung der Quelle erzielt werden. Um präzisere elektrische Messungen durchführen zu können, ist ein Oszilloskop mit erheblich höherer Sample Rate von Nöten. Zudem empfiehlt sich die Verwendung eines RF-Generators und Anpassungsnetzwerks, die speziell für diesen Einsatzbereich konstruiert worden sind. Nichtsdestotrotz erlaubt der derzeitige Entwicklungsstand der Plasma-Nadel ihre Verwendung bei Experimenten auf dem Gebiet der Plasmainteraktion mit biologischem Gewebe und Zellen.

Acknowledgement

I would like to express my sincere gratitude and appreciation to the following people who supported me during this study:

- Prof. Müller-Veggian and Prof. Palmieri for offering me the possibility to write my thesis at the LNL and for their helpful comments and guidance.
- Prof. Schöning for his proofreading.
- Niccolò for his endless patience, support, laughs, and advice during my work.
- Dr. ir. E. Stoffels for her inspirational talk and discussions.
- Dott.ssa Sara Carturan for her support on the FTIR-experiments.
- Dott. Gianluigi Maggioni for his cooperation and assistance on the optical emission spectroscopy.
- Mauro Pignatto for conducting and discussing the ELISA-experiment.
- Finalmente, vorrei ringraziare tutti i ragazzi del laboratorio, nominativo Elena, Giuglia, Judilka, le due Silvia, Vanessa, Antonio, Cristian, Fabio, Fabrizio, Giorgio, Marcel, Niccolò, Nicola, Oscar, Paolo e naturalmente Alessandro e Marigo! Spero che io non ho dimenticato qualcuno.

Bibliography

- [1] E. Stoffels, A. J. Flikweert, W. W. Stoffels, and G. M. W. Kroesen. Plasma-needle: a non-destructive atmospheric plasma source for fine surface treatment of (bio)materials. *Plasma Sources Science and Technology* 11 (2002) 383-388.
- [2] R. E. J. Sladek, and E. Stoffels. Deactivation of *Escherichia coli* by the plasma-needle. *Journal of Physics D: Applied Physics* 38 (2005) 1716-1721.
- [3] E. Stoffels, I. E. Kieft, and R. E. J. Sladek. Superficial treatment of mammalian cells using plasma needle. *Journal of Physics D: Applied Physics* 36 (2003) 2908-2913.
- [4] D. Borg, P. Henley, A. Husain, N. Stroehrer, P. King, and E. Stoffels. Development of a gas plasma catheter for gas plasma surgery. Conference: *XXVIIIth ICPIG, Eindhoven, The Netherlands, 18-22 July, 2005*.
- [5] J. Goree, B. Liu, D. Drake, and E. Stoffels. Killing of *S. mutans* bacteria using a plasma-needle at atmospheric pressure. *IEEE Transactions on Plasma Science* 34 (4) (2006) 1317-1324.
- [6] K. Kelly-Wintenberg, A. Hodge, T.C. Montie, L. Deleanu, D. Sherman, J. R. Roth, P. Tsai, and L. Wadsworth. Use of a one atmosphere uniform glow discharge plasma to kill a broad spectrum of microorganisms. *The Journal of Vacuum Science and Technology A* 17 (4) (1999) 1539-1544 .
- [7] G. Fridman, A. Shereshevsky, M. M. Jost, A. D. Brooks, A. Fridman, A. Gutsol, V. Vasilets, and G. Friedman. Floating electrode dielectric barrier discharge plasma in air promoting apoptotic behaviour in melanoma skin cancer cell lines. *Plasma Chemistry and Plasma Processing* 27 (2) (2007) 163-176.
- [8] J. S. Brinen, S. Greenhouse, and L. Pinatti. ESCA and SIMS studies of plasma Treatments of Intraocular Lenses. *Surface and Interface Analysis* 17(2)(1991) 63-70.
- [9] I. H. Loh, H.-L. Lin, and C. C. Chu. Plasma surface modification of synthetic absorbable sutures. *Journal of Applied Biomaterials* 3 (2) (1992) 131-146.

- [10] S. Yuan, G. Szakalas-Gratzl, N. P. Ziats, D. W. Jacobsen, K. Kottke-Marchant, and R. E. Marchant. Immobilization of high-affinity heparin oligosaccharides to radiofrequency plasma-modified polyethylene. *Journal of Biomedical Materials Research* 27 (6) (1993) 811-819.
- [11] R. K. Roy, and K.-R. Lee. Biomedical applications of diamond-Like carbon coatings: A review. *Journal of Biomedical Materials Research Part B: Applied Biomaterials* 83B (1) (2007) 72-84.
- [12] N. Laube, J. Bradenahl, A. Meißner, J. v. Rappard, L. Kleinen, and S. C. Müller. Plasma-deposited carbon coating on urological indwelling catheters – Preventing formation of encrustations and consecutive complications. *The Journal of Urology* 177 (5) (2007) 1923-1927.
- [13] V. V. Sleptsov, V. M. Elinson, N. V. Simakina, A. N. Laymin, I. V. Tsygankov, A. A. Kivaev, and A. D. Musina. Ophthalmological application of contact lenses modified by means of ion-assisted carbon films. *Diamond and Related Materials* 5 (1996) 483–485.
- [14] V. M. Elinson, V. V. Sleptsov, A. N. Laymin, V. V. Potraysay, L. N. Kostuychenko, and A. D. Moussina. Barrier properties of carbon films deposited on polymer-based devices in aggressive environments. *Diamond and Related Materials* 8 (1999) 2103–2109.
- [15] K. Gutensohn, C. Beythien, J. Bau, T. Fenner, P. Grewe, R. Koester, K. Padmanaban, and P. Kuehnl. In vitro analyses of diamond-like carbon coated stents: Reduction of metal ion release, platelet activation and thrombogenicity. *Thrombosis Research* 99 (2000) 577-585.
- [16] A. Dorner-Reisel, C. Schürer, and E. Müller. The wear resistance of diamond-like carbon coated and uncoated Co₂₈Cr₆Mo knee prostheses. *Diamond and Related Materials* 13 (2004) 823-827.
- [17] C. Tendero, C. Tixier, P. Tristant, J. Desmaison, and P. Leprince. Atmospheric pressure plasmas: A review. *Spectrochimica Acta Part B* 61 (2006) 2-30.
- [18] H. Conrads, and M. Schmidt. Plasma generation and plasma sources. *Plasma Sources Science and Technology* 9 (2000) 441-454.

- [19] T. Schwarz-Sellinger, A. von Keudell, and W. Jacob. Plasma chemical vapor deposition of hydrocarbon films: The influence of hydrocarbon source gas on the film properties. *Journal of Applied Physics*, 86 (7) (1999) 3988-3996.
- [20] S. Rudakowski. Diagnostik an einer gepulsten RF-Entladung zur Erzeugung dünner a-C: H Schichten. Dissertation an der Ruhr-Universität Bochum, Fakultät für Physik und Astronomie, 2002.
- [21] B. Lipschultz, I. Hutchinson, B. LaBombard, and A. Wan. Electric probes in plasmas. *The Journal of Vacuum Science and Technology A* 4 (3) (1986) 1810-1816.
- [22] C. Fanara and I. M. Richardson. A Langmuir multi-probe system for the characterization of atmospheric pressure arc plasmas. *Journal of Physics D: Applied Physics* 34 (2001) 2715-2725.
- [23] R. M. Clements. Plasma diagnostics with electric probes. *The Journal of Vacuum Science and Technology* 15 (2) (1978) 193-198.
- [24] M. Klindworth. Fundamentals and applications of Langmuir probe diagnostics in complex plasmas. Dissertation an der Christian-Albrechts-Universität Kiel, Mathematisch-Naturwissenschaftliche Fakultät, 2004.
- [25] V. Léveillé, and S. Coulombe. Electrical probe calibration and power calculation for a miniature 13.56 MHz plasma source. *Measurement Science and Technology* 17 (2006) 3027-3032.
- [26] R. W. B. Pearse, and A. G. Gaydon. The identification of molecular spectra *Chapman and Hall, London*, 4th edition (1976).
- [27] I. E. Kieft, E. P. v. d. Laan, and E. Stoffels. Electrical and optical characterization of the plasma-needle. *New Journal of Physics* 6 (149) (2004) 1-14.
- [28] I.-S. Bae, S.-H. Cho, Z. T. Park, J.-G. Kim, and J. H. Boo. Organic polymer thin films deposited on silicon and copper by plasma-enhanced chemical vapor deposition method and characterization of their electrochemical and optical properties. *The Journal of Vacuum Science and Technology A* 23 (4) (2005) 875-879.

- [29] J. Benedikt, K. Focke, A. Yanguas-Gil, and A. von Keudell. Atmospheric pressure microplasma jet as a depositing tool. *Applied Physics Letters* 89 (25) (2006) 1-3.

List of tables

Tab. 1:	Classification of different diamond-like carbon films.....	15
Tab. 2:	Heat conductivity of different gases	19
Tab. 3:	Calculation of cyclohexane content.....	34
Tab. 4:	Peak voltage, peak current, and phase shift.....	52
Tab. 5:	Results of contact angle measurements	64
Tab. 6:	Settings for ELISA experiment	64

List of figures

Fig. 1:	Crystal lattice of diamond (left) and crystal lattice of graphite (right).....	14
Fig. 2:	Ternary phase diagram of amorphous carbon	15
Fig. 3:	Dependence between plasma temperature and pressure.....	19
Fig. 4:	Paschen's curves for different gases.....	20
Fig. 5:	Preliminary experiments with microwaves	23
Fig. 6:	Microwave driven plasma-jet formation at higher power	24
Fig. 7:	Microwave generated plasma protruding from the cylinder.....	24
Fig. 8:	Equivalent circuitry of a coaxial cable	26
Fig. 9:	Schematic sketch of the plasma-needle	30
Fig. 10:	Schematic sketch of the device and its electrical connection.....	31
Fig. 11:	Schematic of the gas flow.....	31
Fig. 12:	Pure helium plasma at 25W	32
Fig. 13:	Helium plasma with admixture of 35sccm cyclohexane at 25W	32
Fig. 14:	Self-made power meter.....	35
Fig. 15:	Schematic of the voltage probe.....	36
Fig. 16:	Schematic of the electric circuitry with attached voltage probe.....	38
Fig. 17:	Typical Langmuir probe characteristic.....	39
Fig. 18:	Droplet on a surface forming a contact angle.....	41
Fig. 19:	Plasma treatment of microtiter plate.....	43
Fig. 20:	Sample loaded on profilometer.....	44
Fig. 21:	Typical FTIR spectra of lead nitrate (upper) and glycerine (lower).....	45
Fig. 22:	Schematic illustration of an FTIR spectrometer.....	46
Fig. 23:	Constructive interference of two beams	47
Fig. 24:	Superposition of two beams.....	47
Fig. 25:	Destructive interference of two beams	48
Fig. 26:	Three light beams of different wavelength.....	48
Fig. 27:	Superposition of three light beams	48
Fig. 28:	U-I characteristic of the plasma-needle device for a pure helium plasma....	50
Fig. 29:	Typical measured waveforms	51
Fig. 30:	Current and voltage signals after smoothing and peak determination.....	52
Fig. 31:	Temperature as function of distance between the needle-tip and the surface of the thermometer for a pure helium plasma	55
Fig. 32:	Temperature as function of power for a pure helium plasma.....	56
Fig. 33:	Temperature of helium discharges with admixture of cyclohexane.....	57
Fig. 34:	Emission spectrum of the plasma-needle for a pure helium plasma	58
Fig. 35:	Emission spectrum of a helium-cyclohexane plasma.....	59
Fig. 36:	Thin copper untreated (left) and treated (right)	62

Fig. 37:	Thick copper untreated (left) and treated (right)	62
Fig. 38:	Silicon untreated (left) and treated (right)	62
Fig. 39:	Quartz untreated (left) and treated (right).....	63
Fig. 40:	Millipore petri dish untreated (left) and treated (right)	63
Fig. 41:	Polymer-like hydrogenous amorphous carbon deposited on silicon untreated (left) and treated (right).....	63
Fig. 42:	ELISA results.....	65
Fig. 43:	Example of a deposited film (left), same example with inverted colours (right)	66
Fig. 44:	Profiles of different films deposited at 20 W and 35 sccm cyclohexane.....	67
Fig. 45:	Profiles of different films deposited at 20 W and 7 sccm cyclohexane.....	68
Fig. 46:	FTIR-spectrum of an a-C:H film deposited in air	69
Fig. 47:	FTIR spectra of two a-C:H films deposited in different atmospheres.....	70
Fig. 48:	Reduction of oxygen-containing groups.....	71

Appendix

Permission to use copyrighted material:

Guten Tag Herr Bäcker,

Sie dürfen diese Bilder mit Angabe der Quelle "Fraunhofer IST" gerne für Ihre Diplomarbeit verwenden. Sie sind in hoher Auflösung auf www.kohlenstoffschichten.de unter "Download" erhältlich.

*Mit freundlichen Grüßen
Jan Gäbler*

--

*Dr.-Ing. Jan Gäbler, Fraunhofer-Institut für Schicht- und Oberflächentechnik IST
Abteilung Diamanttechnologie, Projektleiter
Bienroder Weg 54 E, 38108 Braunschweig, Germany
Telefon: + 49 (0) 5 31 / 21 55 - 6 25
<mailto:jan.gaebler@ist.fraunhofer.de>
<http://www.ist.fraunhofer.de>*

Abschließende Erklärung

Ich versichere hiermit, dass ich meine Diplomarbeit ‚Development and characterization of a plasma-needle for biomedical applications‘ selbstständig und ohne fremde Hilfe angefertigt habe, und dass ich alle Quellen zitiert habe.

Padua, den 13. September 2007